

On the Ocean Conditions of Hycean Worlds

Frances E. Rigby¹^{*} and Nikku Madhusudhan¹[†]

¹*Institute of Astronomy, University of Cambridge, Madingley Road, Cambridge CB3 0HA, UK*

Accepted 29th January 2024. Received 26th January 2024; in original form 9th October 2023.

ABSTRACT

Recent studies have suggested the possibility of Hycean worlds, characterised by deep liquid water oceans beneath H₂-rich atmospheres. These planets significantly widen the range of planetary properties over which habitable conditions could exist. We conduct internal structure modelling of Hycean worlds to investigate the range of interior compositions, ocean depths and atmospheric mass fractions possible. Our investigation explicitly considers habitable oceans, where the surface conditions are limited to those that can support potential life. The ocean depths depend on the surface gravity and temperature, confirming previous studies, and span 10s to ~1000 km for Hycean conditions, reaching ocean base pressures up to ~6×10⁴ bar before transitioning to high-pressure ice. We explore in detail test cases of five Hycean candidates, placing constraints on their possible ocean depths and interior compositions based on their bulk properties. We report limits on their atmospheric mass fractions admissible for Hycean conditions, as well as those allowed for other possible interior compositions. For the Hycean conditions considered, across these candidates we find the admissible mass fractions of the H/He envelopes to be ≤10⁻³. At the other extreme, the maximum H/He mass fractions allowed for these planets can be up to ~4-8%, representing purely rocky interiors with no H₂O layer. These results highlight the diverse conditions possible among these planets and demonstrate their potential to host habitable conditions under vastly different circumstances to the Earth. Upcoming JWST observations of candidate Hycean worlds will allow for improved constraints on the nature of their atmospheres and interiors.

Key words: exoplanets – planets and satellites: interiors – planets and satellites: composition – planets and satellites: oceans

1 INTRODUCTION

Earth is the only environment in the universe known to host life. Therefore it is logical that the search for habitable exoplanets and biosignatures began by focusing on Earth-like, rocky exoplanets (e.g. [Kasting et al. 1993](#); [Meadows & Barnes 2018](#); [Ramirez 2018](#)). However the rapidly increasing number and diversity of detected exoplanets has prompted wider considerations for habitability studies and candidates for biosignature detections (e.g. [Madhusudhan et al. 2021](#)). Another related element is identifying conducive targets for atmospheric characterisation and biosignature detections based on our current and upcoming facilities. The sub-Neptune regime spans planets with radii ~1 – 4 R_⊕, between those of Earth and Neptune. The larger sizes of sub-Neptunes compared to small, rocky, Earth-like exoplanets makes these planets more conducive to atmospheric characterisation via transit spectroscopy. Similar interest arises for planets transiting M dwarfs (e.g. [Wunderlich et al. 2019](#); [Tremblay et al. 2020](#)). Numerous sub-Neptunes transiting bright (J < 10 mag) M dwarfs have been discovered by recent transit surveys (e.g. [Ricker et al. 2015](#); [Günther et al. 2019](#); [Hardegree-Ullman et al. 2020](#); [Cloutier et al. 2020](#)). Spectroscopic observations of these planets with the James Webb Space Telescope (JWST) provide exciting opportunities for detailed atmospheric characterisation and the potential for biosignature searches (e.g. [Madhusudhan et al. 2023b](#)).

A new type of habitable exoplanet within the sub-Neptune regime was recently proposed by [Madhusudhan et al. \(2021\)](#), known as Hycean worlds. These temperate planets are characterised by their deep H₂O oceans and H₂-rich atmospheres, and provide a new avenue for habitability studies. The impetus for Hycean worlds came from the study of the habitable-zone sub-Neptune K2-18 b ([Madhusudhan et al. 2020](#)). By coupling atmosphere and interior models, they placed constraints on the composition and surface conditions of K2-18 b, finding that this planet could host liquid water at its surface beneath an H₂-rich atmosphere. Hycean worlds were shown to broaden the commonly considered limits of habitability, in mass, radius, temperature and orbital distance. Due to their H₂ atmospheres, the Hycean habitable zone is significantly wider than the terrestrial habitable zone. Importantly, both the larger size and larger atmospheric scale height of Hyceans relative to rocky planets of similar mass make them more promising targets for atmospheric spectroscopy and potential biosignature detections. Recent analysis of JWST transmission spectra of K2-18 b by [Madhusudhan et al. \(2023b\)](#) revealed strong detections of both CH₄ and CO₂, with a lack of key molecules including NH₃, suggesting the presence of a surface ocean, based on chemical arguments ([Yu et al. 2021](#); [Hu et al. 2021](#); [Tsai et al. 2021](#); [Madhusudhan et al. 2023a](#)). We are in the exciting position where detailed atmospheric data for multiple temperate sub-Neptunes orbiting M dwarfs is soon to be accessible, with observations already being carried out in Cycle 1 (for example, K2-18 b in GO programs 2722 and 2372), with more sub-Neptune targets being observed in other programs in Cycles 1 and 2.

^{*} E-mail: fer29@ast.cam.ac.uk

[†] E-mail: nmadhu@ast.cam.ac.uk

Internal structure modelling plays an important role in characterising sub-Neptunes, relating observable properties to possible interior compositions (e.g. Rogers & Seager 2010b; Valencia et al. 2013; Dorn et al. 2017; Madhusudhan et al. 2020; Nixon & Madhusudhan 2021; Huang et al. 2022). The sub-Neptune population is thought to contain a diverse range of interior compositions with varying proportions of volatiles including H₂O and H/He, with volatile-rich and volatile-poor populations separated by the radius valley (e.g. Fulton et al. 2017). One of the key challenges in internal structure modelling of sub-Neptunes is compositional degeneracy, with a range of compositions usually able to explain a planet’s observed mass and radius. In the era of JWST, interior constraints can be drastically improved via information revealed about exoplanet atmospheres, allowing us to gain more insight into the nature of these planets than ever before. Atmospheric observations provide the key in breaking the aforementioned degeneracies between possible interior compositions (Madhusudhan et al. 2020). For example, the presence of a steam atmosphere can be ruled out and an H₂-rich atmosphere can be established through transmission spectroscopy (e.g. Benneke et al. 2019; Tsiaras et al. 2019; Madhusudhan et al. 2020; Mikal-Evans et al. 2023). Even having established the presence of an H₂-rich atmosphere, Hycean compositions can be degenerate with rocky worlds with thick H/He envelopes, and with mini-Neptunes with large fractions of ices – see Figure 1 in Madhusudhan et al. (2023a). Precise atmospheric data can allow the possible identification of Hycean worlds among the sub-Neptune population. Based on photochemical models, Madhusudhan et al. (2023a) outlined a framework for diagnosing a Hycean world using retrieved chemical abundances, considering the effect of the surface ocean on the atmospheric composition. Notably in recent work, Madhusudhan et al. (2023b) infer the possibility of a liquid H₂O surface on Hycean candidate K2-18 b.

The interiors of Hycean worlds can possess substantial fractions of H₂O, up to 90% by mass (Madhusudhan et al. 2021), compared to ~0.02% for the Earth (Genda 2016). Accurate internal structure modelling of H₂O-rich planets, including Hycean worlds, requires taking into account the thermal behaviour of H₂O across the complex phase diagram (e.g. Thomas & Madhusudhan 2016; Mousis et al. 2020; Huang et al. 2021; Nixon & Madhusudhan 2021). This is achieved via a pressure and temperature dependent equation of state (EOS), which tends to be compiled from several data sources valid for different phases and/or regions of *P-T* space (e.g. Thomas & Madhusudhan 2016; Nixon & Madhusudhan 2021; Haldemann et al. 2020). At high pressures H₂O forms high-pressure ices, which would occur deep in Hycean interiors – specifically, these are ice VI, VII and ice X (Noack et al. 2016; Nixon & Madhusudhan 2021). The behaviour of high-pressure ices remains uncertain due to a lack of extensive experimental data, which can affect the accuracy of internal structure models for water-rich planets (e.g. Huang et al. 2021).

Several recent studies have investigated the internal structures and ocean depths of temperate water-rich sub-Neptunes. Nixon & Madhusudhan (2021) conducted internal structure modelling to examine the H₂O phase structure across a wide range of masses, compositions and surface conditions of such planets. Other studies have also explored the range of ocean depths on sub-Neptunes, under more specific assumptions (e.g. Léger et al. 2004; Sotin et al. 2007; Alibert 2014; Noack et al. 2016). For instance, Alibert (2014) investigated cases avoiding high-pressure ice layers, and Sotin et al. (2007) assumed a fixed surface temperature of 300 K. The results of Nixon & Madhusudhan (2021) highlight the wide range of parameter space over which liquid water could exist at the surface of a planet, which suggests a diverse range of planets could host Hycean conditions. They also investigated the key factors in determining ocean depth,

finding this to be surface gravity and ocean base pressure (and hence surface temperature, due to the adiabatic temperature structure), and constrained the range of ocean depths possible across a wide phase space as functions of these.

In this study, we focus on Hycean worlds, requiring habitable pressures and temperatures at the interface between the ocean and the H₂-rich atmosphere. Based on previous studies, we expect the depths to reach hundreds of times the depth on Earth. For example, Nixon & Madhusudhan (2021) find that depending on the planet’s interior composition and mass, at surface temperatures of 300 K a planet can host oceans between 30 – 500 km deep. Similarly, depths of ~100 – 400 km were found to be possible for the canonical Hycean world based on K2-18 b in Madhusudhan et al. (2023a), assuming habitable surface conditions. Given the significant H₂O mass fractions expected in Hycean worlds the ocean base would occur at the transition to high-pressure ice, as opposed to a rocky ocean floor as on Earth, which could have implications for their habitability (Maruyama et al. 2013; Noack et al. 2016; Journaux et al. 2020b; Madhusudhan et al. 2023a). For example, the thick mantle of high-pressure ice on Hycean worlds would prevent the weathering of the rocky core below, necessitating alternative methods of nutrient enrichment in the oceans. Madhusudhan et al. (2023a) explored the possible chemical conditions on Hycean worlds, identifying feasible pathways to concentrate bioessential elements in Hycean oceans. These include atmospheric condensation, external delivery and convective transport from the rocky core across the ice mantle.

The lack of sub-Neptunes in our own solar system and the ubiquity of exoplanets in this regime mean that there is a wealth of information to be gained from their study, on planet formation and evolution, in addition to habitability. The radius valley is the observed dearth of planets in the radius range ~1.5 – 2 R_⊕, which separates two subpopulations with bimodal peaks at ~1.4 R_⊕ and ~2.4 R_⊕ (Fulton et al. 2017; Fulton & Petigura 2018; Petigura 2020). The low radius peak is commonly accepted to be largely rocky super-Earths, while the characteristics of the planets in the second peak remain debated, and link to their formation/evolution mechanism. The position of the radius valley is dependent on both orbital period and stellar mass (Fulton & Petigura 2018), with the trend with stellar insolation reversing for M dwarfs compared to more massive stars (Cloutier & Menou 2020). Formation mechanisms for the radius valley remain debated, and fall broadly into two categories. The first category relies on atmospheric mass loss, such that super-Earths are the envelope-stripped remnants of mini-Neptunes without large water ice fractions – i.e. largely rocky cores with an H₂-rich atmosphere (e.g. Lopez et al. 2012; Owen & Wu 2013; Gupta & Schlichting 2019; Rogers & Owen 2021). Two methods of mass loss are generally considered, photoevaporation (e.g. Owen & Wu 2013, 2017) and core-powered (e.g. Gupta & Schlichting 2019). The second category places a larger emphasis on inherent differences in composition, with the larger radius peak containing planets with large H₂O components (e.g. Zeng et al. 2019; Mousis et al. 2020; Venturini et al. 2020; Izidoro et al. 2022). The nature and formation of the sub-Neptune population remains an open question, with the permitted mass fraction for an H₂-rich atmosphere of a sub-Neptune varying by the assumed formation/evolution mechanism. Identifying the envelope mass fractions of the sub-Neptune population is hence important in testing these mechanisms. Furthermore, constraining the composition requirements of Hycean worlds is an important step for investigating the formation/evolution pathway for this class of planet, which has yet to be studied in detail.

In this study we present an analysis of the possible conditions on Hycean worlds using a selection of Hycean candidates due to be observed with JWST, including TOI-270 d, TOI-732 c, TOI-1468 c,

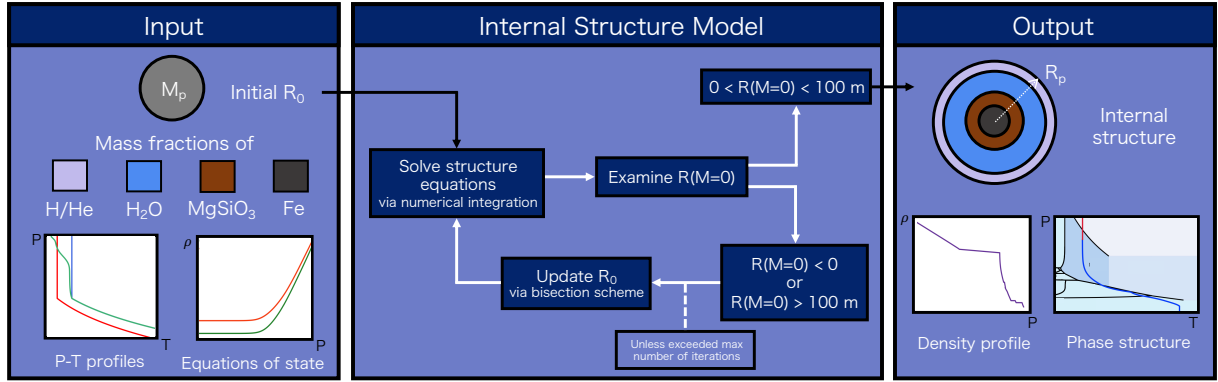


Figure 1. Diagram of the HyRIS internal structure code architecture. The code takes inputs of planetary mass and the mass fractions of its interior layers, and solves the planetary structure equations via numerical integration to output the planet radius. Equations of state and P - T profiles are adopted for each layer.

K2-18 b and LHS 1140 b. We use our internal structure model to estimate the range of possible ocean depths for these planets as Hycean worlds, and the maximum mass fraction in H/He to allow habitable conditions. We consider another end-member scenario, of a rocky planet with a deep H_2 -rich atmosphere and no ocean, to constrain the overall upper limit for H/He mass fraction. We discuss the implications of the envelope mass fractions for sub-Neptune formation/evolution, and the effects of Hycean conditions on the observable properties of these planets.

2 METHODS

In this section we present an internal structure model for sub-Neptunes, HyRIS, with special application to Hycean worlds. We first describe the model and the functionality of the code. The specific assumptions made for our purpose of studying candidate Hycean worlds are outlined. These include the adopted equation of state (EOS) and temperature profile used to describe each planetary component layer.

2.1 Internal Structure Model

Over the past two decades, a number of studies have developed internal structure models to study planetary interiors (e.g. Léger et al. 2004; Fortney et al. 2007; Seager et al. 2007; Sotin et al. 2007; Valencia et al. 2007; Rogers & Seager 2010a; Madhusudhan et al. 2012; Zeng & Sasselov 2013; Thomas & Madhusudhan 2016; Brugger et al. 2017; Madhusudhan et al. 2020; Nixon & Madhusudhan 2021; Huang et al. 2022). Here we describe HyRIS, our internal structure model for sub-Neptunes, and how this is customised for the study of Hycean worlds.

The model solves the planetary structure equations under the assumption of spherical symmetry. The planetary structure equations are the mass continuity equation,

$$\frac{dR}{dM} = \frac{1}{4\pi R^2 \rho} \quad (1)$$

and the equation for hydrostatic equilibrium,

$$\frac{dP}{dM} = -\frac{GM}{4\pi R^4} \quad (2)$$

where for a spherical shell, R is the radius, M is the mass enclosed,

ρ is the density and P is the pressure. The EOS gives the density as a function of pressure and temperature, $\rho = \rho(P, T)$. The choice of EOS and temperature profile, $T = T(P)$, for each layer are outlined in Sections 2.2 and 2.3. In the default set-up of HyRIS, four differentiated layers are considered – a H/He envelope, a pure H_2O layer, a silicate mantle and an iron core, as are commonly considered for sub-Neptunes (e.g. Rogers & Seager 2010a; Madhusudhan et al. 2020; Nixon & Madhusudhan 2021).

In a similar method to Nixon & Madhusudhan (2021), the structure equations are solved using a fourth-order Runge-Kutta numerical integration procedure. The boundary conditions are chosen to be at the planet’s surface since these are associated with atmospheric observables. The model solves for the planet radius R_p , taking inputs of planet mass M_p , mass fractions of its constituents $x_i = M_i/M_p$, and photospheric pressure P_0 and temperature T_0 . If no envelope is included, the boundary P_0 and T_0 will be at the planet’s surface. The integration procedure works inwards from the outside of the planet, stepping through decreasing enclosed mass M , where the size of mass step dM is adjusted according to the current M and ρ . R_p is obtained via a bisection root-finding method with a convergence condition of a radius value of less than 100 m at zero enclosed mass, $0 < R(M=0) < 100$ m. In addition to R_p and the thickness of each planetary layer, the interior density profile and H_2O phase structure can be output if required. The model architecture is summarised in Figure 1.

The EOSs adopted for the different materials are described in Section 2.2. However HyRIS is flexible, with the nature of each planetary layer and the associated EOS able to be easily modified. For instance, miscibility of the H_2O and H/He layers can be included (e.g. Section 4.2). See Section 4.3 for further discussion of possible developments and adaptations to the model.

2.1.1 Exploring Hycean conditions

For this study, HyRIS has been customised to explore the parameter space for Hycean worlds, and facilitate quick extraction of useful quantities. We automate the extraction of 1σ solutions of internal structures for the M_p and R_p measurements for a given planet from a large number of interior model executions across the full parameter space of possible mass fractions. We further automate the determination of Hycean solutions from the 1σ solutions. As discussed above, the model can output the density profile and H_2O phase structure, along with the R_p and thickness of each planetary layer. For a

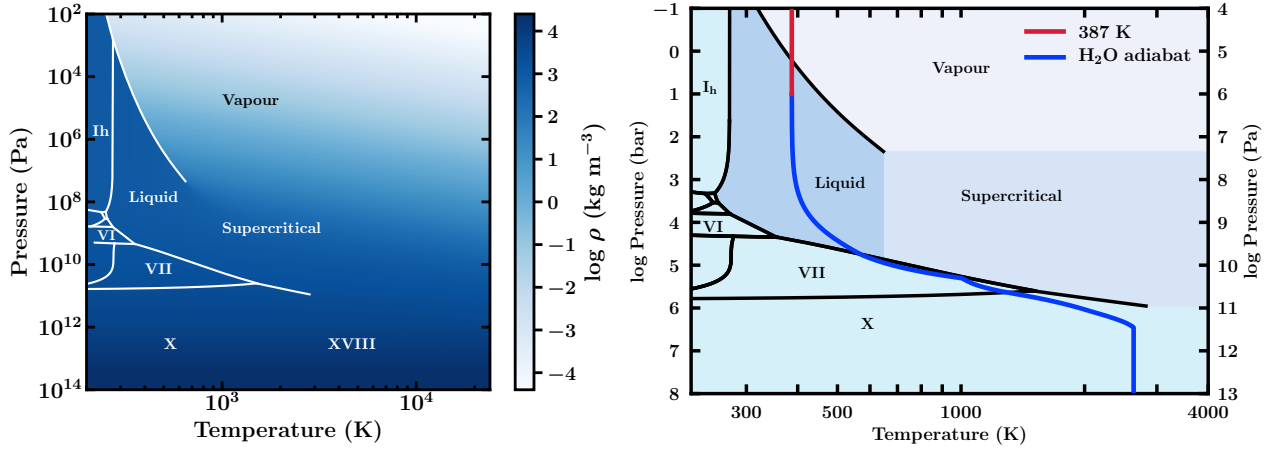


Figure 2. Left: Phase diagram and EOS for H₂O used in our model. The phase diagram is constructed from [Dunaeva et al. \(2010\)](#) and [Wagner & Pruß \(2002\)](#), and the sources for the EOS are outlined in Table 1. Right: Example H₂O adiabat with HHB at 387 K and ~ 10 bar. This is the profile for the possible interior of TOI-270 d shown in Figure 10, with 387 K the equilibrium temperature with $A_B = 0$ for TOI-270 d. The red line shows the atmospheric profile, which follows an isotherm at these pressures. The black lines and background shading show the phase diagram of H₂O.

Table 1. Sources and regions of validity for the components of our H₂O EOS, shown in Figure 2.

EOS and Source	Validity
IAPWS-1995, (Wagner & Pruß 2002)	Vapour, liquid, supercritical
French et al. (2009)	Supercritical, ice VII, ice X, ice XVIII, plasma. 1000 – 24000 K, $1.86 \times 10^9 - 9.87 \times 10^{12}$ Pa
Feistel & Wagner (2006)	Ice Ih. 0 – 273 K, 0 – 10 ⁸ Pa
Journaux et al. (2020a)	Ices II, III, V, VI
Fei et al. (1993)	Ice VII
Fei et al. (1993) , Klotz et al. (2017)	Ice VIII
Thomas-Fermi-Dirac (TFD), (Salpeter & Zapolsky 1967)	$P > 7.686 \times 10^{12}$ Pa
Seager et al. (2007)	Remaining high-pressure regions
IAPWS-1995 extrapolation, (Wagner & Pruß 2002)	Remaining regions, (low-pressure and high-temperature vapour)

given solution, if the surface is found to lie in the liquid phase of H₂O, the ocean depth is calculated. For Hyceans, with liquid surfaces with temperatures up to ~400 K, the base of the ocean will be high-pressure ice. Hotter surfaces can lead to supercritical oceans, as shown in [Nixon & Madhusudhan \(2021\)](#).

2.2 Equations of State

For each planetary layer considered which are typically H/He, H₂O, silicates and iron, we require an EOS to describe the pressure and temperature dependent density variation within each layer. We describe the choice of EOS for each layer and, where relevant, the process to compile them.

2.2.1 H₂O

We use a temperature-dependent EOS for pure H₂O, compiled following a similar approach to [Thomas & Madhusudhan \(2016\)](#) and [Nixon & Madhusudhan \(2021\)](#). Our EOS is valid for temperatures in

the range 200 – 24000 K and pressures 10² – 10²² Pa (10⁻³ – 10¹⁷ bar). It is comprised of a number of different sources valid for certain phases and/or regions of P - T space. These sources will be described below, and are summarised in Table 1. We use phase-boundaries from [Dunaeva et al. \(2010\)](#), in addition to the liquid-vapour boundary from [Wagner & Pruß \(2002\)](#).

For the liquid and vapour phases and some parts of the supercritical phase, we use the EOS from the International Association for the Properties of Water and Steam (IAPWS) ([Wagner & Pruß 2002](#)), referred to as the IAPWS-1995 formulation. This EOS has been well tested experimentally. We use the functional form of the IAPWS-1995 formulation, which is calculated directly from the Helmholtz free energy, to give pressure as a function of density and temperature, $P = P(\rho, T)$. This requires a bounded root-finding procedure to be carried out to obtain $\rho = \rho(P, T)$ for each phase.

We use the EOS of [French et al. \(2009\)](#), the data for which covers multiple phases, including supercritical, high-pressure ices (ice VII, X and XVIII) and plasma. This EOS is based on quantum molecular dynamics simulations, and has since been experimentally validated by [Knudson et al. \(2012\)](#). The EOS for remaining regions of the supercritical phase is an extrapolation of the IAPWS-1995 EOS.

For the majority of ice VII (the high-temperature region is covered by the [French et al. \(2009\)](#) EOS), we use a functional EOS in the form of a Vinet EOS with a thermal correction from [Fei et al. \(1993\)](#). The Vinet EOS is given by

$$P = 3B_0\eta^{\frac{2}{3}} \left(1 - \eta^{-\frac{1}{3}}\right) \exp\left[\frac{3}{2} \left(B'_0 - 1\right) \left(1 - \eta^{-\frac{1}{3}}\right)\right] \quad (3)$$

where $\eta = \rho/\rho_0$, ρ_0 is the ambient density, $B_0 = \rho (\partial P/\partial \rho)|_T$ is the isothermal bulk modulus and B'_0 its pressure derivative. The thermal correction is given

$$\rho(P, T) = \rho_0(P, T_0) \left[\exp\left(\int_{T_0}^T \alpha(P, T) dT\right) \right]^{-1} \quad (4)$$

where T_0 is the ambient temperature, here 300 K ([Fei et al. 1993](#)). The thermal expansion coefficient α here is

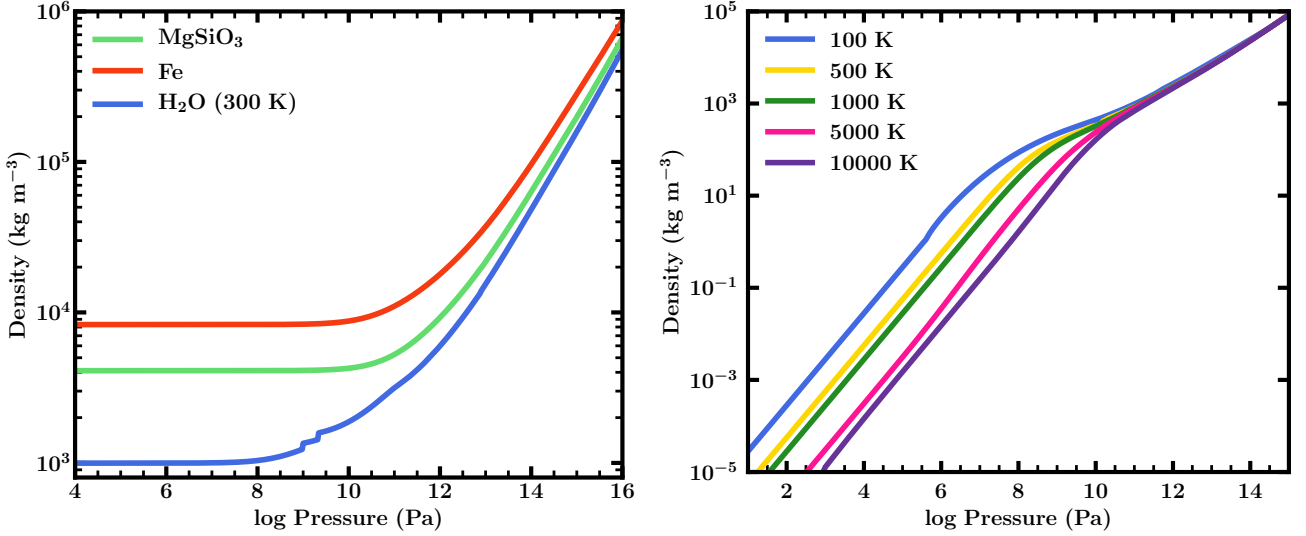


Figure 3. Left: The temperature-independent EOS for each of MgSiO₃ and Fe used in our model (from Seager et al. 2007). The equivalent EOS for H₂O from Seager et al. (2007) is also shown for comparison. Right: The EOS for H/He used in our model (from Chabrier et al. 2019), shown for different isotherms.

$$\alpha(P, T) = \alpha_0(T) \left[1 + \frac{B'_0}{B_0} P \right]^{-\eta} \quad (5)$$

where $\alpha_0(T)$ is a linear function of T , and η is a constant (Fei et al. 1993). The coefficients were experimentally determined via x-ray diffraction (Fei et al. 1993). Via an alternative form of α_0 from Klotz et al. (2017), we also extrapolate this EOS to cover ice VIII.

For ice Ih we use the functional form of the EOS from Feistel & Wagner (2006). Ices II, III, V and VI are also covered by experimental data, from Journaux et al. (2020b) via the SeaFreeze package.

At high pressures, above 7.686×10^7 bar (7.686×10^{12}) Pa we adopt a modified Thomas-Fermi-Dirac (TFD) EOS as in Salpeter & Zapolsky (1967). This EOS is temperature independent, due to the minimal effect of temperature in this regime. There remains an intermediate region in pressure space between ice VII and X not covered by experimental data or the TFD EOS. In this region we use the H₂O EOS from Seager et al. (2007). This is comprised of three regimes – at lower pressures this is a Birch-Murnaghan (BM) EOS (Birch 1952) with coefficients from Hemley et al. (1987), transitioning to density functional theory results with increasing pressure, and finally to a TFD at high pressures.

Our full H₂O EOS and phase diagram are shown in Figure 2. The EOS was constructed based on the regions of validity described above and in Table 1. This is either via the phase boundaries, or by the bounds of the data.

We validate our H₂O EOS against the EOS of Nixon & Madhusudan (2021). We expect these to be almost identical due to the sources used. In Figure 5 we show this to be the case, showing the density as a function of pressure for different isotherms.

For c_p , required for the adiabatic gradient (see Section 2.3), we use the same sources as the EOS where available (for Wagner & Pruß 2002; Feistel & Wagner 2006; Journaux et al. 2020a). For regions where there is no data for c_p , we adopt the c_p value of the nearest available point in P - T space. α is determined directly from the EOS, as in Equation 8.

Table 2. Values used in the EOSs for the iron and silicate layers, from Anderson et al. (2001) and Karki et al. (2000) respectively.

Layer	B_0 (GPa)	B'_0	B''_0 (GPa ⁻¹)	ρ (kg m ⁻³)
Fe	156.2	6.08	N/A	8300
MgSiO ₃	247	3.97	-0.016	4100

2.2.2 Silicates and iron

Since thermal effects within the core and mantle have been found to have a minimal effect on the planetary M - R relation (e.g. Grasset et al. 2009), we adopt an isothermal EOS in the silicate mantle and iron core, as is frequently assumed in other internal structure models (e.g. Rogers et al. 2011; Thomas & Madhusudan 2016). For this we use the EOS from Seager et al. (2007). These EOSs are shown in Figure 3.

The iron core is described by a Vinet EOS (Vinet et al. 1989; Anderson et al. 2001) for hexagonal close-packed Fe, before similarly transitioning to a TFD EOS (Salpeter & Zapolsky 1967) at higher pressures.

For the silicate layer, assumed to be the perovskite phase of MgSiO₃, the EOS is in the form of a fourth-order BM EOS (Birch 1952; Karki et al. 2000), and a TFD EOS (Salpeter & Zapolsky 1967) at high pressure. The BM EOS is described by

$$P = \frac{3}{2} B_0 \left(\eta^{\frac{7}{3}} - \eta^{\frac{5}{3}} \right) \left[1 + \frac{3}{4} (B'_0 - 4) \left(\eta^{\frac{2}{3}} - 1 \right) + \frac{3}{8} B_0 \left(\eta^{\frac{2}{3}} - 1 \right)^2 \left[B_0 B''_0 + B'_0 (B'_0 - 7) + \frac{143}{9} \right] \right] \quad (6)$$

where B''_0 is the second pressure derivative of the isothermal bulk modulus. The coefficients for this are from Karki et al. (2000), and are given in Table 2.

2.2.3 Hydrogen/Helium

We assume a solar helium fraction for the H/He envelope ($Y = 0.275$). The EOS from Chabrier et al. (2019) is used, which is valid for

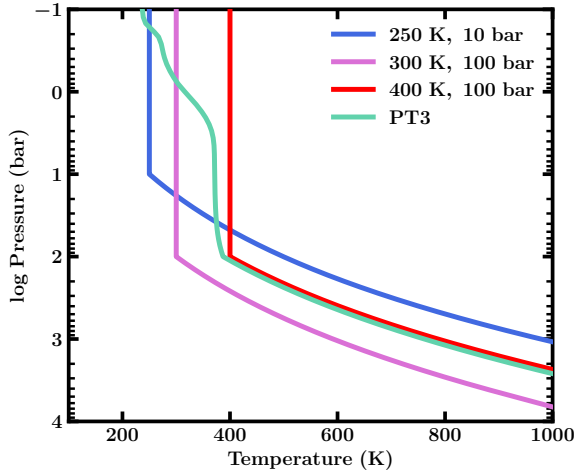


Figure 4. Forms of P - T profile used for the H/He envelope. Example isothermal/adiabatic profiles are shown at three different temperatures with P_{rc} between 10 – 100 bar. PT3 is from Madhusudhan et al. (2023a), generated via self-consistent modelling with GENESIS (Gandhi & Madhusudhan 2017; Piette & Madhusudhan 2020) for K2-18 b.

$1 - 10^{22}$ Pa and $100 - 10^8$ K. This EOS is comprised of models applicable at different density and temperature regimes, and the hydrogen and helium EOSs are combined via an additive-volume law. In our temperature range, the models used are from Saumon et al. (1995); Caillabet et al. (2011); Chabrier & Potekhin (1998) – see Chabrier et al. (2019) for a full description of the model. This EOS is shown in Figure 3.

2.3 Temperature Profiles

The model considers pressure and temperature dependent EOSs. HyRIS can accommodate user-specified P - T profiles for the atmosphere, while in the interior, an adiabatic profile is typically assumed. Madhusudhan et al. (2021) showed that the P - T structure expected in the observable H_2 -rich atmospheres of Hycean worlds around M dwarfs are well approximated by an isothermal profile. We note that the atmospheric compositions of Hycean worlds could be rich in CH_4 and CO_2 (e.g. Madhusudhan et al. 2023b), which could further affect the temperature structure. Nixon & Madhusudhan (2021) also showed that P - T profiles for sub-Neptunes generated via self-consistent atmospheric modelling with GENESIS (Gandhi & Madhusudhan 2017; Piette & Madhusudhan 2020) could be reasonably approximated by isothermal/adiabatic profiles, with the radiative-convective boundary, P_{rc} , lying at $\sim 1 - 1000$ bar. In the H/He atmosphere, we hence assume an isotherm down to $P_{rc} = 100$ bar, with the P - T profile then following an adiabat in the deeper atmosphere. Example profiles are shown in Figure 4.

Under the assumption of vigorous convection, we similarly assume an adiabatic temperature profile in the H_2O layer, as is commonly assumed in internal structure models (e.g. Sotin et al. 2007; Nixon & Madhusudhan 2021; Leleu et al. 2021). An example interior adiabat is shown in Figure 2. The adiabatic profiles are described by the adiabatic temperature gradient,

$$\nabla_{ad} = \left. \frac{\partial T}{\partial P} \right|_S = \frac{\alpha T}{\rho c_p} \quad (7)$$

where α is the coefficient of volume expansion and c_p is the isobaric specific heat capacity. α is derived from the EOS,

$$\alpha = \frac{1}{V} \left. \frac{\partial V}{\partial T} \right|_P = - \left. \frac{\partial \ln \rho}{\partial T} \right|_P \quad (8)$$

where V is the specific volume.

Alternative temperature profiles can be easily included within HyRIS. For instance, atmospheric temperature profiles generated via self-consistent modelling (e.g. Piette & Madhusudhan 2020) can be used in the place of the isothermal/adiabatic profiles. An example of this is carried out for K2-18 b in Section 3.2.4.

2.4 Model Validation

We validate our model against the results of previous studies of sub-Neptune internal structures. In Figure 5 we reproduce M - R relations from Seager et al. (2007) and Nixon & Madhusudhan (2021). The results of our model are shown in black, with the 100% Fe, 100% silicate and Earth-like curves from Seager et al. (2007), and the M - R curves including H_2O from Nixon & Madhusudhan (2021). The Earth-like composition consists of 2/3 silicate and 1/3 iron. The Seager et al. (2007) cases are taken to be isothermal planets, as the EOSs used are temperature-independent. We expect our results to match Seager et al. (2007) due to the use of identical EOSs, which we see. We also see close agreement with the M - R curves from Nixon & Madhusudhan (2021), which represent 30% and 90% H_2O with an Earth-like core. Henceforth, we use “core” to refer to the rocky component of the interior, including both the silicate and iron layers. These cases of 300 K and 1 bar surface were chosen as they are representative of a Hycean interior, with the interior P - T profile following an adiabat as described in Section 2.3. In Section 3.1 we compare our model ocean depth results to those of previous studies.

3 RESULTS

In this section we present our results for the possible oceanic and interior conditions of Hycean worlds. Firstly we validate our model ocean depths against the results of previous studies (Léger et al. 2004; Noack et al. 2016; Nixon & Madhusudhan 2021), before constraining the theoretical range of ocean depths possible on Hycean worlds. We then explore in detail five candidate Hyceans, placing constraints on their possible ocean depths, interior compositions and envelope mass fractions. The envelope mass fractions are determined for the case of a Hycean world and for the case of a rocky world with a thick H/He envelope, the latter representing the overall maximum envelope fraction for these sub-Neptunes.

3.1 Ocean Depths on Hycean Worlds

Hycean worlds are defined to have 10 – 90% H_2O by mass (Madhusudhan et al. 2021), therefore in all calculations we impose these limits on the H_2O mass fraction. To allow for the surface ocean, we require the H/He- H_2O boundary (HHB) to lie at pressures and temperatures that support the liquid phase of H_2O . The HHB is what we will refer to as the “surface”. We further place the constraint of habitable surface conditions, requiring surface temperatures T_{HHB} of 273 – 400 K and pressures P_{HHB} of 1 – 1000 bar, motivated by the range of conditions supporting life on Earth (Rothschild & Mancinelli 2001; Merino et al. 2019). We consider core compositions between Earth-like (33% Fe) and pure Fe. The internal structure model is then applied across the full Hycean phase space, for planets

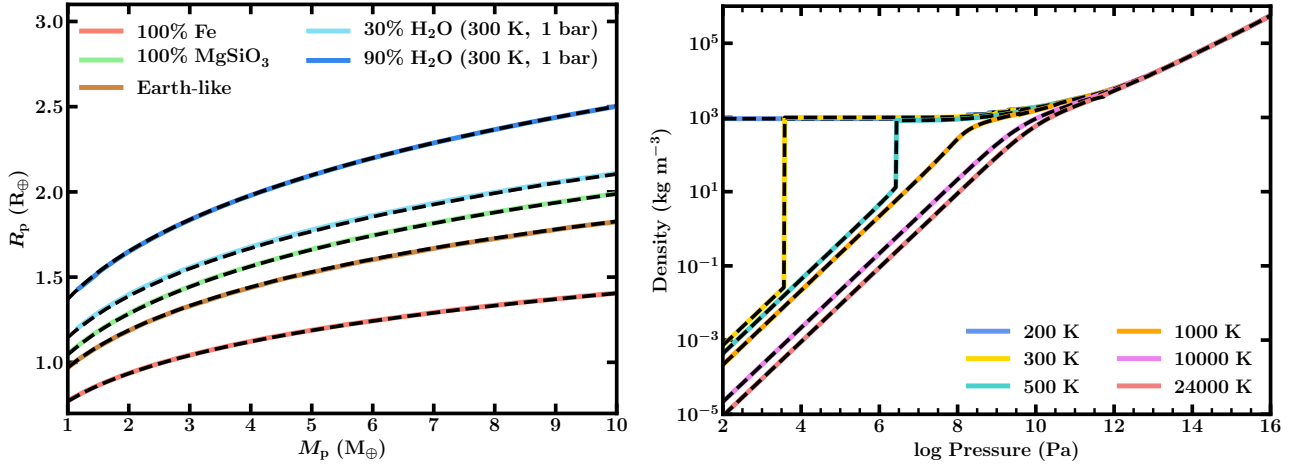


Figure 5. Left: Mass-radius (M - R) relations produced using our model compared to the results of Seager et al. (2007) and Nixon & Madhusudhan (2021). The 100% Fe, 100% MgSiO_3 and Earth-like ($2/3$ MgSiO_3 , $1/3$ Fe) curves are from Seager et al. (2007). The curves with 30% (90%) H_2O and 70% (10%) Earth-like core are from Nixon & Madhusudhan (2021), assuming liquid surfaces at 300 K and 1 bar. The M - R curves produced using our model are shown in black. Right: Comparison of our H_2O EOS to the EOS of Nixon & Madhusudhan (2021), for several isotherms. Our results are shown in black. These results are almost identical due to the identical sources used for the EOS and phase boundary data.

with $1 - 10 M_\oplus$, $10\% \leq x_{\text{H}_2\text{O}} \leq 90\%$, $273 \leq T_{\text{HHB}} \leq 400$ K. For each combination we extract R_p and the ocean depth.

We first reproduce some previous results in the literature. Noack et al. (2016) found that the maximum ocean depth for a planet varies with the mass, composition and surface temperature of the planet. Similarly, Nixon & Madhusudhan (2021) showed that the ocean depth is affected by the surface gravity and ocean base pressure. The pressure at the ocean base, where the transition from liquid to high-pressure ice occurs, is fixed by the interior adiabat and hence the surface temperature. In Figure 6a we reproduce these results using our model, showing the inverse proportionality of ocean depth and surface gravity. The surface pressure is fixed at 100 bar as in Nixon & Madhusudhan (2021) – varying this within a reasonable range ($\sim 1 - 1000$ bar) does not significantly affect the results, in agreement with Nixon & Madhusudhan (2021). In Figure 6b we also show the ocean depth against the HHB temperature for a range of surface gravity values. The change in slope at ~ 295 K corresponds to the transition between an ocean base of ice VI vs ice VII. Nixon & Madhusudhan (2021) showed that peak depths occur for $T_{\text{HHB}} = 413$ K with the trend reversing for $T_{\text{HHB}} > 413$ K (up to the critical temperature). Therefore, as seen in Figure 6, the trend with temperature is straightforward for our considered temperature range of 273 – 400 K, with an increase in T_{HHB} causing an increase in ocean depth. We reiterate that in Figure 6, this is the gravity and temperature at the ocean surface (g_{HHB} , T_{HHB}), not with the envelope included (g_0 , T_0). As an illustration, for a planet with $M_p = 6 M_\oplus$, 50% H_2O , 50% Earth-like core and $T_{\text{HHB}} = 303$ K, we obtain a depth of 127 km. This is in good agreement with the 125 km found by Nixon & Madhusudhan (2021) and 133 km found by Léger et al. (2004).

We find that ocean depths on Hycean worlds can range between 10s of km to ~ 1000 km, depending on the planet’s mass, composition and surface conditions. For comparison, the average depth of Earth’s ocean is 3.7 km (Charette & Smith 2010), with the deepest part (the Mariana trench) extending to ~ 11 km (Gardner et al. 2014). For the theoretical maximum depth of a Hycean ocean, we find ~ 1000 km – this end-member case is a $1 M_\oplus$ planet with 90% H_2O and $T_{\text{HHB}} = 400$ K, i.e. maximal T_{HHB} and minimal $\log(g)$. Conversely,

the minimum depth is ~ 20 km, for a $10 M_\oplus$ planet with 10% H_2O , 90% Fe and $T_{\text{HHB}} = 273$ K.

The calculated ocean depths as a function of surface gravity g and T_{HHB} , as shown in Figure 6, can be used to estimate the range of ocean depths possible for a given planet. For instance, in Figure 6a we show estimates of the ocean depths possible for TOI-270 d, TOI-1468 c and TOI-732 c, shown by the shaded regions. The T_{HHB} range considered is from T_{eq} at $A_B = 0.5$, calculated via Equation 9, up to the maximum of 400 K. Alternatively, using Figure 6b the range of ocean depths can be estimated given a value for the surface gravity. For example, for a surface gravity similar to K2-18 b of $\log g = 3.1$, the range of ocean depths would be $\sim 65 - 380$ km, for HHB temperatures 273 – 400 K. In this method, g is implicitly being assumed as constant throughout the atmosphere. In reality, the gravity for each planet would be higher at the ocean surface than at the photosphere, where R_p is measured from. These represent initial estimates, as not all the solutions in these regions will be permissible for a planet when the gravity in the atmosphere is allowed to vary, and an atmospheric P - T profile adopted; these are considered in Section 3.2.

We also assess the effect of different mass and radius measurements in the literature for a given planet. For this purpose, we consider the planet TOI-732 c for which such measurements are available from three sources as shown in Table 3. In Figure 7 we show the range of ocean depths obtained using the mass and radius values from each of the three sources. The Cloutier et al. (2020) (hereafter referred to as “C20”) range is the same as in Figure 6. If we instead consider the Nowak et al. (2020) values (hereafter referred to as “N20”) we find that somewhat deeper oceans are possible. The more precise measurements of N20 compared to C20 result in a smaller $\log g$ range at lower values, allowing larger depths. Conversely, the similar maximum $\log g$ for Bonfanti et al. (2024) (“B23”) and C20 result in a similar upper limit for ocean depth. The improved precision of the B23 measurements again results in a narrower $\log g$ range and hence a smaller range of ocean depths. We note that the equilibrium temperature is not varied between the three examples, given the similar estimates between the three studies and the surface temperature being

Planet	M_p/M_\oplus	R_p/R_\oplus	$T_{\text{eq},0}/\text{K}$	$T_{\text{eq},0.5}/\text{K}$	a/AU	M_\star/M_\odot	R_\star/R_\odot	T_{eff}/K	V mag	J mag	Refs	
K2-18 b	8.63 ± 1.35	2.610 ± 0.087	297	250	0.153	0.45	0.44	3590	13.48	9.76	1,2	
		$2.51^{+0.13}_{-0.15}$									3	
TOI-732 c	$8.60^{+1.60}_{-1.30}$	$2.30^{+0.18}_{-0.15}$	353	297	0.07673	0.40	0.37	3331	13.14	9.01	4	
		$6.29^{+0.63}_{-0.61}$									2.42 ± 0.10	5
		$8.04^{+0.50}_{-0.48}$									$2.39^{+0.10}_{-0.11}$	6
TOI-1468 c	$6.64^{+0.67}_{-0.68}$	2.064 ± 0.044	338	284	0.0859	0.34	0.34	3496	12.50	9.34	7	
TOI-270 d	4.78 ± 0.43	2.133 ± 0.058	387	326	0.0733	0.39	0.38	3506	12.60	9.10	8,9	
		4.20 ± 0.16									2.19 ± 0.07	10,11
LHS 1140 b	6.98 ± 0.89	1.727 ± 0.032	235	198	0.0936	0.18	0.21	3216	14.15	9.61	12	
		$6.38^{+0.46}_{-0.44}$									1.635 ± 0.046	13
		5.60 ± 0.19									1.730 ± 0.025	226

Table 3. Properties of the Hycean candidates considered in this work. Equilibrium temperature values are calculated with $A_B = 0$ and $A_B = 0.5$, and assuming uniform day-night redistribution. References: 1: Cloutier et al. (2019), 2: Benneke et al. (2019), 3: Hardegree-Ullman et al. (2020), 4: Cloutier et al. (2020), 5: Nowak et al. (2020), 6: Bonfanti et al. (2024), 7: Chaturvedi et al. (2022), 8: Günther et al. (2019), 9: Van Eylen et al. (2021), 10: Mikal-Evans et al. (2023), 11: Kaye et al. (2022), 12: Ment et al. (2019), 13: Lillo-Box et al. (2020), 14: Cadieux et al. (2024).

unconstrained. For example, T_{eq} is $305 - 363$ K for N20 compared to $297 - 353$ K for C20, for $0 \leq A_B \leq 0.5$.

3.2 Case Studies

We now explore in detail the possible range of ocean depths and atmospheric mass fractions for five promising Hycean candidates with upcoming JWST observations. The properties of these planets and their host stars are listed in Table 3. The planets include K2-18 b, TOI-270 d, TOI-1468 c, TOI-732 c and LHS 1140 b. These planets are shown against the Hycean mass-radius (M - R) plane from Madhusudhan et al. (2021) in Figure 8. We estimate the maximum mass fraction in the H/He envelope for these planets for two end-member cases – as a Hycean world, and as a rocky planet with a deep H_2 -rich atmosphere and no H_2O . In the latter case, the maximum density interior of a pure Fe core is assumed in order to obtain the upper limit for H/He mass fraction. We note this is purely an upper limit, as a 100% Fe core is unrealistic by planet formation scenarios. The upper H/He limit has implications for planet formation studies, which is discussed further in Section 3.4.

For each planet, we consider equilibrium temperatures assuming Bond albedos in the range $0 \leq A_B \leq 0.5$. This is motivated by the values of Madhusudhan et al. (2021) – the maximum $A_B = 0.5$ is used for their calculation of the inner habitable zone boundary for Hycean planets, motivated by Selsis et al. (2007); Yang et al. (2013); de Pater & Lissauer (2010). The equilibrium temperature is calculated by

$$T_{\text{eq}} = T_\star \left[\frac{R_\star^2}{2a^2} (1 - A_B) (1 - f_r) \right]^{\frac{1}{4}} \quad (9)$$

where a is the orbital semi-major axis, R_\star and T_\star are the stellar radius and effective temperature respectively, and f_r is the fraction of incident radiation that is redistributed to the nightside. In this work we assume that this redistribution is efficient, adopting $f_r = 0.5$ for uniform day-night energy redistribution, giving a uniform equilibrium temperature across the planet. The Hycean candidates we consider here are expected to be tidally locked. Depending on the efficiency of day-night redistribution, there could be differences between the temperature of the day and night sides. Future work would be needed to study the effects of inefficient day-night redistribution on their interiors and oceans, including the case of Dark Hyceans (Madhusudhan et al. 2021).

In Section 3.1 we assumed constant gravity in the atmosphere, to

demonstrate how initial estimates of the possible ocean depths could be obtained via Figure 6. As described in Section 3.1, the depths in Figure 6 were calculated assuming a fixed P_{HHB} of 100 bar. In the subsequent sections, we discuss individual cases with gravity varying in the atmosphere. We evaluate the internal structure model across the full range of possible layer mass fractions to identify the compositions that satisfy the 1σ range of M_p and R_p , including compositions that allow for Hycean conditions. The P_{HHB} and T_{HHB} are not fixed, with the allowed range for Hycean solutions spanning $273 \leq T_{\text{HHB}} \leq 400$ K and $1 \leq P_{\text{HHB}} \leq 1000$ bar. As described in Section 2.3, the atmospheric P - T profiles are assumed to be isothermal/adiabatic profiles, with $P_{\text{rc}} = 100$ bar. T_0 is taken to span the T_{eq} range between $A_B = 0$ and $A_B = 0.5$, as outlined above. P_0 is taken to be the reference pressure for R_p where available, and otherwise we adopt the reference pressure of 0.05 bar, following Madhusudhan et al. (2020). We consider end-member core compositions of Earth-like (33% Fe) and pure Fe.

3.2.1 TOI-270 d

TOI-270 d is a sub-Neptune discovered with TESS (Günther et al. 2019), with RV follow-ups with ESPRESSO (Van Eylen et al. 2021). The TOI-270 system contains three transiting planets orbiting an M3V host star with near-mean motion resonance, allowing recent transit-timing variations to be detected (Kaye et al. 2022). Both TOI-270 c and TOI-270 d are Hycean candidates (Madhusudhan et al. 2021). TOI-270 d orbits at 0.07 au and has $M_p = 4.20 \pm 0.16 M_\oplus$ (Kaye et al. 2022) and $R_p = 2.19 \pm 0.07 R_\oplus$ (Mikal-Evans et al. 2023). TOI-270 d is hottest of the Hycean candidates we consider in this paper, with T_0 taken to be $326 - 387$ K (this is the T_{eq} range for $0 \leq A_B \leq 0.5$, as outlined above). This planet was recently the subject of an atmospheric study with HST, which suggested an H_2 -rich atmosphere with H_2O absorption (Mikal-Evans et al. 2023). We take P_0 as 0.0912 bar, which is the reference pressure for R_p (Mikal-Evans et al. 2023).

We find the possible Hycean ocean depths for TOI-270 d span $\sim 200 - 500$ km, $\sim 50 - 140$ times the average depth of Earth’s ocean at 3.7 km (Charette & Smith 2010) ($\sim 20 - 50$ times the deepest part at ~ 11 km (Gardner et al. 2014)). As discussed in Section 3.1, the maximal ocean depth is achieved with the minimum surface gravity and maximal surface temperature. In Figure 9 we show an example interior for TOI-270 d with a maximal ocean depth of 500 km. This case has the lower bound $M_p = 4.04 M_\oplus$, with $R_p = 2.22 R_\oplus$. The H_2O mass fraction is at its maximum $x_{\text{H}_2\text{O}} = 90\%$, with $x_{\text{H/He}} =$

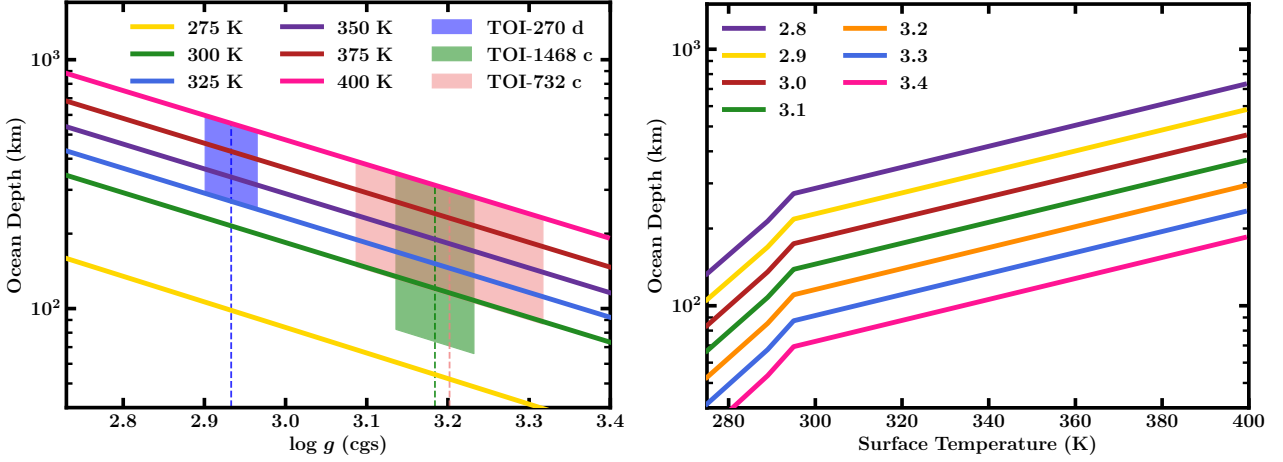


Figure 6. Left (a): Ocean depth against surface gravity for a range of habitable surface temperatures. The shaded regions indicate the estimated range of ocean depths for three Hycean candidates, based on uncertainty in their surface gravity and temperature. The dashed line indicates the median gravity. The mass and radius values adopted for each target are their first entry in Table 3. Right (b): Ocean depth against surface temperature for a range of surface gravity values.

0.011% and the remaining mass in an Earth-like core. The surface temperature lies at the maximum of 400 K, at pressure 112 bar – more than 100 times the surface pressure on Earth. Conversely, an example interior at the lower end of ocean depths has $x_{\text{H}_2\text{O}} = 86\%$, $x_{\text{H}/\text{He}} = 0.0072\%$ and the remainder in an Earth-like core, for $M_p = 4.264 M_\oplus$ and $R_p = 2.13 R_\oplus$. The depth in this case is 221 km, with the HHB at the minimum temperature, 326 K, and 90 bar. We note that the interiors able to achieve a given ocean depth are degenerate. The minimum mass fraction of H_2O required for TOI-270 d to be a Hycean world is found to be 68%. This occurs for a low density interior, with maximum surface temperature 400 K and an Earth-like core composition. These constraints on the H_2O content of sub-Neptunes can be useful for testing planet formation scenarios (e.g. Bitsch et al. 2021).

We require a H/He mass fraction of $\lesssim 0.0195\%$ for TOI-270 d to be a Hycean world. This limit corresponds to the maximal H_2O mass fraction of 90% and an Earth-like core of 9.9815%, with the isothermal temperature in the atmosphere $T_0 = 326$ K. The HHB in this case is 197 bar and at the maximum of 400 K, as an increase in H/He mass fraction would increase the temperature at the surface beyond the habitable range. Conversely, a minimum H/He mass fraction of 1.7×10^{-6} is required for Hycean conditions. This limit occurs for the maximum $T_0 = 387$ K and 90% H_2O and an Earth-like core, giving an HHB at 20 bar and 387 K. Lower H/He mass fractions produce an R_p below the lower 1σ limit.

If we consider our other end-member case of a rocky planet with an H/He envelope, we find a maximum envelope fraction of 6.1%. This is achieved using the lower T_0 of 326 K and a pure Fe core, with no H_2O . An Earth-like core would reduce the maximum H/He fraction to 3.7%, for the same P - T profile.

We have adopted $P_{\text{rc}} = 100$ bar for the H/He envelope. As shown by Nixon & Madhusudhan (2021), the choice of P_{rc} affects the maximum H/He fraction that allows for an HHB within the liquid phase. A lower P_{rc} results in lower permitted H/He fractions, as the atmospheric temperature increases higher in the atmosphere. If we adopt $P_{\text{rc}} = 10$ bar and $P_{\text{rc}} = 1000$ bar, we find $\sim 0.0017\%$ and $\sim 0.0810\%$ as the maximum H/He fractions for Hycean conditions respectively. The overall maximum H/He fraction then varies from 3.4 – 8.3% for P_{rc} from 10 – 1000 bar. A higher P_{rc} would reduce the range of ocean depths possible, as this restricts the range of T_{HHB} to below the

maximum possible of 400 K. Reducing P_{rc} will not significantly affect the range of ocean depths, as we can already reach the maximum $T_{\text{HHB}} = 400$ K with $P_{\text{rc}} = 100$ bar.

3.2.2 TOI-1468 c

TOI-1468 c is a recently discovered sub-Neptune (Chaturvedi et al. 2022) orbiting its M3V host star at 0.0859 au, along with the closer-in, rocky TOI-1468 b. TOI-1468 c has $M_p = 6.64^{+0.67}_{-0.68} M_\oplus$ and $R_p = 2.064 \pm 0.044 R_\oplus$ (Chaturvedi et al. 2022), with T_0 ranging from 284 – 338 K for our A_B range. For TOI-1468 c and the remaining planets, we adopt $P_0 = 0.05$ bar, which is the median reference pressure from Madhusudhan et al. (2020) for K2-18 b.

The possible ocean depths for TOI-1468 c are found to span ~ 60 –310 km. An example internal structure that facilitates a maximal depth of 309 km is shown in Figure 9. This solution has $x_{\text{H}/\text{He}} = 0.0125\%$, $x_{\text{H}_2\text{O}} = 63\%$ and a pure Fe core, for lower bound $M_p = 5.97 M_\oplus$ and upper bound $R_p = 2.108 R_\oplus$. The surface temperature lies close to the habitable maximum, at 397 K, with an envelope T_0 of 284 K. The surface pressure is ~ 300 times Earth’s surface pressure, at 307 bar, while the base of the ocean lies at 6.0×10^4 bar. This case also represents the solution with maximum envelope mass fraction while maintaining Hycean conditions. Overall we find a maximum permitted H/He fraction of 4.3% for non-Hycean conditions – this is lower than for TOI-270 d due to the higher bulk density of TOI-1468 c. For an Earth-like core, as opposed to a pure Fe core, the maximum H/He mass fraction is 1.8%.

Unlike TOI-270 d, TOI-1468 c is not permitted to have 90% H_2O , again due to its higher bulk density, with the maximum $x_{\text{H}_2\text{O}}$ found to be $\sim 75\%$. The minimum mass fraction of H_2O required for TOI-1468 c to be a Hycean world is found to be 24%. Using this minimum mass fraction of H_2O , we find the lower bound for high-pressure ice thickness on TOI-1468 c (while maintaining Hycean conditions) to be $0.42 R_\oplus$, or ~ 2700 km. Even in this case, the ocean is still very deep, at 230 km. The thickness of the high-pressure ice layer on Hycean worlds could have implications for their habitability, which is discussed further in Section 4.1.

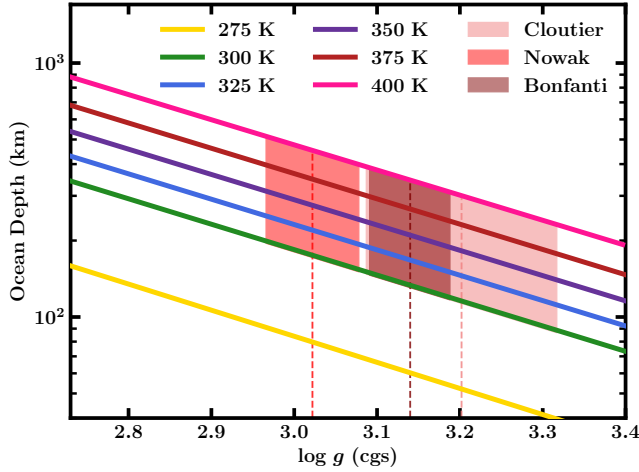


Figure 7. Ocean depth against surface gravity for a range of habitable surface temperatures. The three possible ranges for TOI-732 c for the alternative mass and radius measurements (Cloutier et al. 2020; Nowak et al. 2020; Bonfanti et al. 2024) are shown by the shaded regions.

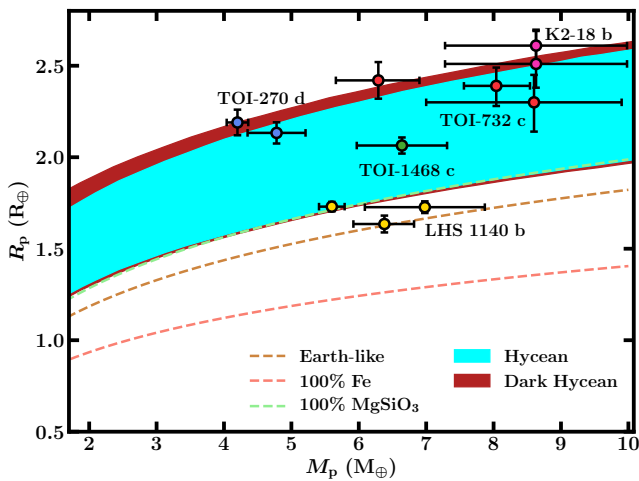


Figure 8. Hycean mass-radius plane from Madhusudhan et al. (2021). The Hycean candidates discussed are also shown – different mass/radius measurements for each planet are shown in corresponding colours.

3.2.3 TOI-732 c

TOI-732 c, or LTT 3780 c, is a sub-Neptune orbiting an M4V host star discovered by TESS, with independent follow-ups with HARPS & HARPS-N (Cloutier et al. 2019) and CARMENES (Nowak et al. 2020). Most recently, combined analysis of TESS, CHEOPS and ground-based light curves was carried out by Bonfanti et al. (2024), along with RV analysis with MAROON-X. This system also contains a super-Earth, TOI-732 b, making this system an interesting test of radius valley formation around M dwarfs (Cloutier et al. 2019). TOI-732 c orbits its host star at 0.08 au (Cloutier et al. 2019; Nowak et al. 2020), giving equilibrium temperatures in the range 284–353 K for our A_B range. Multiple measurements of mass and radius are reported for TOI-732 c, with the masses varying significantly. Cloutier et al. (2020) find $M_p = 8.60^{+1.60}_{-1.30} M_\oplus$ and $R_p = 2.30^{+0.16}_{-0.15} R_\oplus$ while Nowak et al. (2020) find $M_p = 6.29^{+0.63}_{-0.61} M_\oplus$ and $R_p = 2.42 \pm$

$0.10 R_\oplus$. The most recent mass measurement by Bonfanti et al. (2024) is in best agreement with Cloutier et al. (2020), at $M_p = 8.04^{+0.50}_{-0.48} M_\oplus$, with $R_p = 2.39^{+0.10}_{-0.11} R_\oplus$. These are shown by the blue points in Figure 8. In the following calculations and Figure 6, we adopt the Cloutier et al. (2020) values (hereafter referred to as “C20”).

We find possible Hycean ocean depths to range from $\sim 90 - 360$ km. An example internal structure with depth 350 km is shown in Figure 9. This case, with $M_p = 7.10 M_\oplus$ and $R_p = 2.41 R_\oplus$, has $x_{\text{H/He}} = 0.0132\%$, $x_{\text{H}_2\text{O}} = 80\%$ and the remainder in an Earth-like core. The surface temperature lies close to the maximum value at 399 K, with a pressure of 270 bar, for $T_0 = 297$ K. We find a maximum H/He fraction of 0.0142% for TOI-732 c under Hycean conditions. As for TOI-270 d, this is achieved with a maximal H_2O fraction of 90% with 9.986% in a pure Fe core, and a minimal T_0 , here 297 K. The overall maximum H/He fraction for non-Hycean conditions is found to be 6.8%, using the lower T_0 of 297 K and a pure Fe core. A maximum envelope fraction of 3.8% is permitted for an Earth-like core. TOI-732 c has the largest range of permitted H_2O fractions of the planets considered, due to the larger uncertainty in its mass. The minimum mass fraction of H_2O required for TOI-732 c to be a Hycean world is found to be 22%, and the interior in Figure 9 demonstrates solutions are possible up to 90% H_2O .

As shown in Section 3.1, assuming constant gravity in the atmosphere, different mass measurements for TOI-732 c can affect the possible range of ocean depths. Adopting the Nowak et al. (2020) values (“N20”) in our full evaluation of the model (assuming the same range for T_{eq} as used for C20), the maximum depth is found to be 415 km, compared to 350 km for the C20 case. This difference is smaller than Figure 7 would suggest, due to the surface conditions permitted by the results of possible compositions. The maximum H/He fraction is found to be higher than for C20, at 8.2%. For Hycean conditions, the maximum H/He fraction for N20 values is only slightly higher, at 0.0186%.

3.2.4 K2-18 b

We revisit K2-18 b, a well-studied sub-Neptune (e.g. Benneke et al. 2017; Cloutier et al. 2019; Benneke et al. 2019; Tsiaras et al. 2019; Madhusudhan et al. 2020; Blain et al. 2021; Madhusudhan et al. 2023b) and the first Hycean candidate (Madhusudhan et al. 2020, 2021). K2-18 b orbits its M3V host star at 0.15 au, and has $M_p = 8.63 \pm 1.35 M_\oplus$ (Cloutier et al. 2019) and $R_p = 2.610 \pm 0.087 R_\oplus$ (Benneke et al. 2019), or $R_p = 2.51^{+0.13}_{-0.18} R_\oplus$ (Hardegree-Ullman et al. 2020). We use the former R_p value for consistency with previous studies (Madhusudhan et al. 2020). As listed in Table 3, T_{eq} varies between 250 K and 297 K at $A_B = 0.5$ and 0 respectively.

We first adopt PT3 from Madhusudhan et al. (2023a), shown in Figure 4. This profile was generated via self-consistent atmospheric modelling with the GENESIS framework (Gandhi & Madhusudhan 2017; Piette & Madhusudhan 2020) – see Madhusudhan et al. (2023a) for a full description. This profile was calculated to a pressure of 100 bar at which it has temperature 387 K, and we extend to $P > 100$ bar with an adiabatic profile. We note that this profile is different to those used by Madhusudhan et al. (2020) in their internal structure modelling of K2-18 b. They adopt two atmospheric P - T profiles, also generated with GENESIS, which vary in assumptions, including internal temperature. These have $T_{\text{int}} = 25$ K and $T_{\text{int}} = 50$ K, while PT3 from Madhusudhan et al. (2023a), used in this work, has $T_{\text{int}} = 30$ K; see Madhusudhan et al. (2020) and Madhusudhan et al. (2023a) for full descriptions of the assumptions made.

Using PT3, we find the possible ocean depths to be 140 – 350 km. The T_{HHB} range possible using PT3 is limited, since at the minimum P_{HHB} of 1 bar, PT3 is at 316 K. To be a Hycean world, we find K2-18 b requires a H/He fraction of $\lesssim 0.0052\%$. Madhusudhan et al. (2020) find permitted envelope fractions of 0.006% for an interior solution with a liquid surface, consistent with our result. Overall we obtain a maximum H/He fraction of 8.1% for non-Hycean conditions, with a pure Fe core. In comparison, Madhusudhan et al. (2020) found 6.2% for the maximum H/He mass fraction. For an Earth-like core composition, we find a lower maximum H/He fraction of 4.9%.

If we instead adopt isothermal/adiabatic profiles as we have for the other case studies, we expect the aforementioned importance of the atmospheric P - T profile to affect the results. At pressures $\gtrsim 1$ bar PT3 is at higher temperatures than the isothermal/adiabatic cases at $T_0 = 250$ K and $T_0 = 297$ K. Therefore, we find that a larger H/He fraction is permitted for the isothermal/adiabatic case. We adopt $T_0 = 250$ K, which is consistent with the isothermal profile found in the photosphere via the retrieval carried out by Madhusudhan et al. (2023b). As with previous case studies, we adopt $P_{\text{rc}} = 100$ bar. We find a maximum H/He fraction for Hycean conditions of 0.022% for this $T_0 = 250$ K and $T_{\text{HHB}} = 400$ K. In this case, the range of ocean depths is also affected as lower values of T_{HHB} are accessible with this P - T profile. For example, an interior with upper bound M_{p} , $x_{\text{H/He}} = 0.0045\%$, $x_{\text{H}_2\text{O}} = 86\%$ and the remainder an Earth-like core results in a nearly minimal depth of 54 km, at $T_{\text{HHB}} = 277$ K and $P_{\text{HHB}} = 139$ bar. The pressure at the base of the ocean in this case is 1.0×10^4 bar, compared to $\sim 6 \times 10^4$ bar for a 400 K surface. The upper depth limit is not significantly affected by a variation in atmospheric P - T profile as the upper limit for T_{HHB} and hence ocean base pressure is unchanged. Reducing T_0 can allow for even larger H/He mass fractions while maintaining Hycean conditions. For instance, adopting $T_0 = 200$ K results in a maximum H/He mass fraction of 0.046% for Hycean conditions, about twice that for $T_0 = 250$ K. In this case, the HHB lies close to the maximum for habitable conditions, at ~ 1000 bar.

We note that the depth estimates depend strongly on the HHB conditions, which in turn depend on the temperature structure and atmospheric composition. The non-detection of H_2O in the photosphere of K2-18 b may be consistent with the presence of a tropospheric cold trap, with the temperature and H_2O abundance potentially higher in the lower atmosphere (Madhusudhan et al. 2023b). However, it is difficult to accurately estimate the composition and temperature structure of the dayside atmosphere, and the corresponding surface temperature and pressure, based on observed photospheric properties at the day/night terminator using transmission spectroscopy. We have, therefore, considered a wide range for the T_{HHB} for K2-18 b, similar to the other planets in this study, to consistently explore the full range of possibilities.

Across all the P - T profiles considered for K2-18 b the ocean depths span ~ 50 – 350 km. However, the non-detection of H_2O in K2-18 b (Madhusudhan et al. 2023b) may limit the surface temperatures to well below 400 K. We therefore evaluate the possible ocean depths for a lower maximum T_{HHB} of 340 K. Adopting PT3 as the atmospheric profile for this case, we find a narrow ocean depth range of 140 – 180 km. Adopting an isothermal/adiabatic profile at $T_0 = 250$ K and $P_{\text{rc}} = 100$ bar, we find a range of ~ 50 – 180 km. As mentioned previously, given the same maximum T_{HHB} , the upper depth limit is not significantly affected by variations in atmospheric P - T profile. However, the lower depth limit is affected as a lower T_{HHB} , down to 273 K, is possible for the latter P - T profile. Similarly, considering an even lower maximum T_{HHB} further decreases the maximum ocean depth possible, e.g. to ~ 50 – 120 km for 300 K maximal T_{HHB} for

the isothermal/adiabatic profile. Reducing the maximum T_{HHB} also decreases the maximum possible H/He mass fractions for Hycean conditions. For instance, using the isothermal/adiabatic profile the maximum H/He fraction is approximately halved for a maximum T_{HHB} of 340 K compared to 400 K, at $\sim 0.011\%$ vs 0.022%.

3.2.5 LHS 1140 b

Finally, we discuss the case of LHS 1140 b (Dittmann et al. 2017; Ment et al. 2019; Lillo-Box et al. 2020; Cadieux et al. 2024). This planet has a low equilibrium temperature of 235 K for $A_{\text{B}} = 0$ (198 K for $A_{\text{B}} = 0.5$), orbiting its M4.5V host star at 0.0936 au (Ment et al. 2019). Until recently, LHS 1140 b would only have been considered a Hycean candidate for H_2O mass fractions below 10% (Madhusudhan et al. 2021). However, the bulk properties of planet have been revised recently with $M_{\text{p}} = 5.60 \pm 0.19 M_{\oplus}$ and $R_{\text{p}} = 1.730 \pm 0.025 R_{\oplus}$ (Cadieux et al. 2024). These latest measurements place LHS 1140 b within the Hycean M - R plane, and is close to the upper density limit for Hycean candidates, as shown in Figure 8 along with the previously reported measurements. For reference, Ment et al. (2019) reported values $M_{\text{p}} = 6.98 \pm 0.89 M_{\oplus}$ and $R_{\text{p}} = 1.727 \pm 0.032 R_{\oplus}$, placing this planet just outside the upper density limit for Hycean candidates. On the other hand, Lillo-Box et al. (2020) reported $M_{\text{p}} = 6.38^{+0.46}_{-0.44} M_{\oplus}$ and $R_{\text{p}} = 1.635 \pm 0.046 R_{\oplus}$. Madhusudhan et al. (2021) explain that the lower boundary could be closer to the M - R curve for an Earth-like composition if lower H_2O mass fractions were permitted – the minimum is assumed to be 10%, as in this study. LHS 1140 b therefore represents an end-member case, in density and temperature, for Hycean candidates.

We first use the Ment et al. (2019) values, as the most conservative case. We adopt the equilibrium temperature $T_0 = 235$ K and a P - T profile in the envelope with P_{rc} at 100 bar. Even for this conservative case, large ocean depths are possible. For instance, fractions of $x_{\text{H}_2\text{O}} = 30\%$, $x_{\text{H/He}} = 8.0 \times 10^{-5}$ and remainder pure Fe results in a 145 km ocean. The surface temperature is 360 K in this case. Therefore, LHS 1140 b demonstrates that even planets on the extreme boundaries of being candidate Hycean worlds under certain conditions could host 100s of km deep oceans. If we instead use the latest Cadieux et al. (2024) values for M_{p} and R_{p} , giving a lower surface gravity, we find significantly deeper oceans are possible for LHS 1140 b, up to ~ 300 km. For example, mass fractions of $x_{\text{H}_2\text{O}} = 50\%$, $x_{\text{H/He}} = 0.021\%$ and remainder in pure Fe can result in a 290 km ocean, for $T_{\text{HHB}} = 400$ K. This is calculated adopting the same atmospheric P - T profile as used with the Ment et al. (2019) values. If we instead assume an atmospheric profile with the lower $T_0 = 198$ K and $P_{\text{rc}} = 100$ bar, we obtain the maximum H/He fraction for Hycean conditions to be 0.036%. Conversely, for non-Hycean conditions, the maximum H/He fraction is found to be 4.2%, using the same P - T profile and the Cadieux et al. (2024) values, with a pure Fe core. For an Earth-like core, the maximum H/He fraction is reduced to 1.7%.

3.3 Envelope Mass Fractions on Hycean Worlds

The requirements of a habitable ocean places limits on the possible mass fraction of the H/He envelope in a given Hycean world. The envelope mass fraction depends on the temperature structure and the HHB conditions at the ocean surface. Generally, lower atmospheric temperatures allow for higher envelope mass fractions. For example, higher P_{rc} and lower T_0 allow for higher envelope mass fractions, and vice versa. Across our case studies and the assumptions considered in this work we find the maximum envelope mass fractions

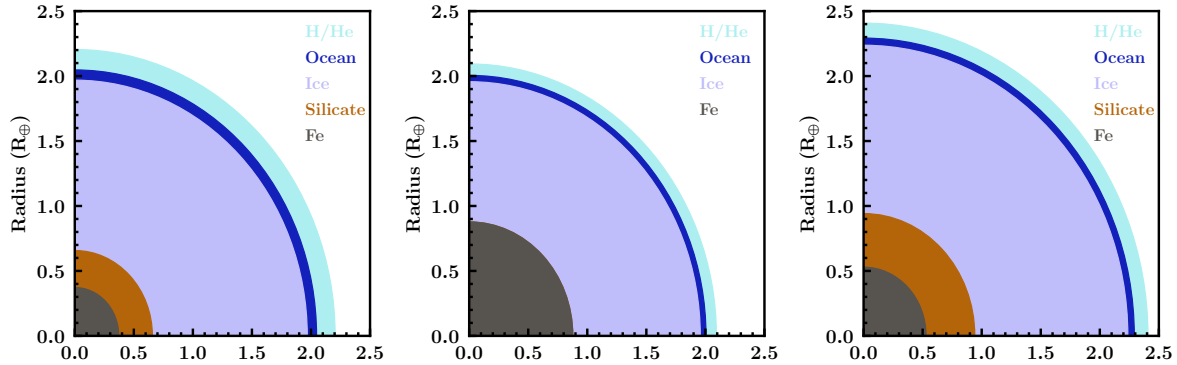


Figure 9. Possible interiors of candidate Hycean worlds. a: TOI-270 d, with ocean depth 500 km. b: TOI-1468 c, with ocean depth 309 km. This case has a pure Fe core, which is likely unrealistic based on planet formation mechanisms. c: TOI-732 c, with ocean depth 350 km.

admissible for Hycean conditions to be $\sim 10^{-3}$. Higher envelope mass fractions correspond to cooler atmospheric temperatures and higher surface pressures. Improved constraints on H/He mass fraction can be obtained via better constraints on the atmospheric temperature structure. Atmospheric observations, for instance with the JWST, are essential for obtaining these improved constraints (e.g. Mikal-Evans et al. 2023; Madhusudhan et al. 2023b). See Section 4.4 for further discussion of upcoming observations.

Presently, the formation mechanisms of Hycean worlds with such envelope mass fractions have not been investigated in detail. More generally, several mechanisms have been proposed for the formation and evolution of sub-Neptune planets, especially with the aim of explaining the radius valley (Fulton et al. 2017; Fulton & Petigura 2018). These mechanisms include processes where thick primordial H_2 -rich envelopes are depleted via photoevaporative mass loss (e.g. Owen & Wu 2017) and/or core-powered mass loss (e.g. Gupta & Schlichting 2019), as well as processes involving outgassing of H_2 from the interiors (e.g. Elkins-Tanton & Seager 2008). Other mechanisms suggest the preponderance of sub-Neptunes with water-rich interiors and envelopes of varied compositions (e.g. Zeng et al. 2019; Venturini et al. 2020; Izidoro et al. 2022), which could include Hycean worlds. Considering photoevaporative and core-powered stripping of the envelopes of sub-Neptunes with 1:1 silicate-to-ice ratios, Rogers et al. (2023) find envelope mass fractions of $\gtrsim 10^{-3}$ can be retained, at $T_{\text{eq}} = 300$ K, after 5 Gyr of photoevaporative evolution. Izidoro et al. (2022) find that water-rich sub-Neptunes with H_2 -rich atmospheres, which could include Hyceans, can be formed via gas-driven migration models, both with and without the inclusion of photoevaporative mass loss. However, the possible envelope mass fractions were not constrained in this study – a fixed fraction of 0.3% was assumed, based on Zeng et al. (2019). Such mechanisms could have varying implications for formation of Hycean planets.

We note that an H_2 -rich envelope mass fraction of $\sim 10^{-4} - 10^{-3}$ is $10^2 - 10^3 \times$ larger than that of the Earth, albeit with a lower mean molecular weight. These required mass fractions open a new avenue for investigating the origins of Hycean worlds. In principle, these mass fractions are at the limit of what could be retained by mass loss mechanisms in temperate sub-Neptunes based on recent studies (e.g. Owen & Wu 2017; Gupta & Schlichting 2019; Rogers et al. 2023). On the other hand, whether outgassing (e.g. Elkins-Tanton & Seager 2008) or other atmosphere/ocean exchange processes can result in these mass fractions remains to be seen.

3.4 Maximum Envelope Mass Fractions

We have additionally placed constraints on the maximum envelope mass fraction for each of the sub-Neptunes we consider. The extreme case assumes a pure Fe interior with no H_2O , with our standard $P_{\text{rc}} = 100$ bar in the envelope. We find that the upper envelope fractions are all within ~ 4 -8%. This is similar to the $\lesssim 7\%$ found by Valencia et al. (2013) for the well-studied GJ 1214 b. The maximum fraction found by Madhusudhan et al. (2020) for K2-18b is also similar, at $\sim 6\%$. For an Earth-like core composition, we find the maximum H/He envelope mass fractions to span ~ 2 -5%.

The upper limit for envelope mass fraction has implications for planet formation and evolution scenarios in the sub-Neptune regime. Mechanisms of atmospheric mass loss, including both photoevaporative (e.g. Owen & Wu 2013, 2017; Rogers & Owen 2021) and core-powered (e.g. Gupta & Schlichting 2019, 2020), make predictions for permitted envelope mass fractions for sub-Neptunes. Determining these for a range of sub-Neptunes including those within and outside of the radius valley can help to test the predictions of these theories. For instance, the photoevaporative scenario (Owen & Wu 2017) predicts mass fractions of order $\sim 1\%$ are typical for envelope-retaining sub-Neptunes. More recent studies also including core-powered mass loss suggest larger mass fractions up to $\sim 10\%$ are possible, depending on the planet mass and radius (Rogers et al. 2023). Our range of derived H/He mass fractions are consistent with these estimates.

4 SUMMARY AND DISCUSSION

In this paper we investigate the range of conditions possible in the interiors of Hycean worlds, including their ocean depths, interior compositions and envelope mass fractions. Our results follow previous works on ocean depths in water-rich sub-Neptunes (Noack et al. 2016; Nixon & Madhusudhan 2021), focusing specifically on Hycean conditions and several candidate Hycean worlds. Firstly, we find the expected range of ocean depths to extend from 10s of km to ~ 1000 km for Hycean worlds. The depth of a Hycean ocean is influenced by the surface conditions, specifically the temperature and gravity, and is hence sensitive to the planet mass, composition, and assumed temperature profile in the envelope. We constrain the possible ocean depths and compositions for a sample of five promising Hycean candidates with upcoming JWST data: TOI-270 d, TOI-1468 c, TOI-732 c, K2-18 b and LHS 1140 b. Secondly, we constrain the mass fractions of the possible H/He envelopes for all the candidates considered. Across the sample we find the maximum envelope fraction admissible for

Hycean conditions to be $\sim 10^{-3}$, for the atmospheric temperature structures explored in this work. Finally, we also constrain the maximum H/He envelope mass fraction for non-Hycean conditions, i.e. for the limiting case of a rocky core with a thick H/He envelope but no H₂O layer. The corresponding envelope mass fractions are found to span $\sim 4 - 8\%$ across the sample.

Our results demonstrate the diverse conditions possible among Hycean worlds, and reinforce their possibility to host habitable conditions under vastly different circumstances to the Earth. The information we expect to gain on atmospheric composition with JWST will provide an indication if these planets could indeed be Hycean worlds and allow us to place better constraints on the nature of their interiors and oceans. With JWST, the detection of possible biomarkers in the atmospheres of Hycean candidates remains an exciting and potentially imminent prospect. The study by Madhusudhan et al. (2023b) of K2-18 b is an exciting first look into the capability of JWST to shed light on this regime.

4.1 Habitability of Hycean Worlds

The habitability of a Hycean world depends on a range of factors. In Figure 10 we show an example of a possible ocean cross-section for the planet TOI-270 d. The maximum depth of Earth’s ocean is shown by the dashed line, at ~ 11 km (Gardner et al. 2014). Life in Earth’s oceans spans the entire depth, down to pressures of ~ 1000 bar (Rothschild & Mancinelli 2001; Merino et al. 2019). As we have shown in Section 3, the depth of Hycean oceans can span hundreds of km down to pressures of $\sim 10^4 - 10^5$ bar ($10^9 - 10^{10}$ Pa) where the transition to ice VI or VII occurs. In this example in Figure 10, the ocean base pressure is at 5.5×10^4 bar. Therefore, the majority of the ocean exists at temperatures and pressures greater than those known to host life on the Earth. We define the “habitable depth” as the depth at which we reach $P = 1000$ bar and/or $T = 400$ K. In this example in Figure 10, the habitable depth is 20 km, where we reach 1000 bar (at 394 K), for an HHB at ~ 10 bar and 387 K. The habitable depth in this case is approximately double the deepest point of Earth’s ocean. Assuming the same surface gravity and temperature, an HHB at lower pressure would result in a larger habitable depth, due to the dependence of depth on the change in pressure. However, changing the HHB pressure within our permitted range makes little difference to the overall ocean depth, which is evident from the rapid increase of pressure with depth shown in Figure 10. We should also note that it is unknown whether life could evolve to exist in conditions beyond these Earth-based pressures and temperatures, extending the potentially habitable portion of the ocean.

Hycean planets are generally expected to have high-pressure ice layers beneath their oceans. The presence of an icy mantle separating the ocean from the rocky core may have implications for the habitability of water-rich bodies (Maruyama et al. 2013; Noack et al. 2016; Journaux et al. 2020b; Madhusudhan et al. 2023a). For instance, the prevention of silicate weathering has been suggested to affect geochemical cycling (e.g. Kitzmann et al. 2015). However, alternative mechanisms have already been proposed for ocean worlds with higher mean molecular weight atmospheres which can also possess high-pressure ice layers (Kite & Ford 2018; Levi et al. 2017; Ramirez & Levi 2018). The geochemical cycles that would occur in Hycean environments are unknown (Madhusudhan et al. 2021) and future work is needed to investigate these possibilities.

The implications of high-pressure ice layers have also been discussed in the context of ocean nutrient enrichment (e.g. Noack et al. 2016; Madhusudhan et al. 2023a). The lack of contact between the ocean and mantle prevents the weathering of the seafloor that can

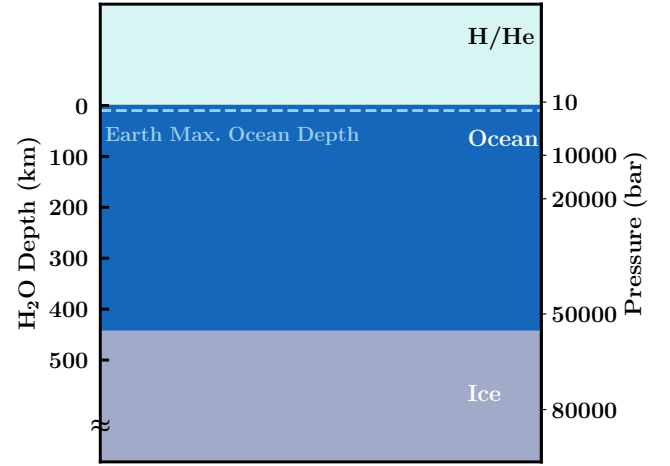


Figure 10. 1-dimensional cross-section of a possible ocean of TOI-270 d. This corresponds to a case with ocean depth 443 km. The maximum ocean depth on Earth is shown as a dashed line, at 11 km.

enrich the ocean with nutrients needed for life. Madhusudhan et al. (2023a) suggest alternative ways to meet the chemical requirements for life in Hycean oceans, including atmospheric condensation and external delivery from asteroids/comets. However, transport across high-pressure ice layers has also been suggested as a possibility, based on a number of works studying convection in the high-pressure ices that could be present on water-rich exoplanets (Choblet et al. 2017; Kalousová et al. 2018; Kalousová & Sotin 2018; Hernandez et al. 2022; Lebec et al. 2023; Madhusudhan et al. 2023a), along with work on icy moons (e.g. Lingam & Loeb 2018; Journaux et al. 2020b). The cases shown in Section 3 have high-pressure ice layers that can generally extend for $\geq 1 R_{\oplus}$. As is intuitive, a smaller mass of H₂O results in a thinner high-pressure ice layer. For example, as discussed in Section 3.2.2, for TOI-1468 c we find the ice can be as thin as $0.42 R_{\oplus}$ for an interior with the minimum permitted mass fraction of H₂O, while still maintaining an ocean depth of 189 km. The thinner the ice layer, the smaller the distance required to transport nutrients across. However, the behaviour of high-pressure ices is largely unknown, including potential interactions between high-pressure ice and the underlying rock (e.g. Journaux et al. 2020b), and future investigation is required to address these areas.

Our Hycean candidates orbit M dwarfs, which are generally more active than higher mass stars. Effects such as stellar wind and higher UV flux are able to erode a planet’s atmosphere, which has the potential to make environments hostile to life (e.g. Shields et al. 2016). However, the level at which a planet will be inhospitable is thought to be significantly dependent on the atmospheric composition and the level of host star activity (e.g. O’Malley-James & Kaltenecker 2017). As pointed out by Madhusudhan et al. (2021), Hycean planets may be more habitable than terrestrial planets around M dwarfs due to their larger gravity and thicker atmospheres. Furthermore, for instance, TOI-270 has been shown by multiple studies (Günther et al. 2019; Van Eylen et al. 2021; Mikal-Evans et al. 2023) to have low stellar activity levels. LTT 3780 (TOI-732) has also been found to be relatively inactive (Nowak et al. 2020; Cloutier et al. 2020), as has TOI-1468 (Chaturvedi et al. 2022). Therefore, these Hycean candidates may stand to be among the more promising candidates for life around M dwarfs. Nevertheless, habitability remains a complex

topic and a rigorous assessment would need to be made on a planet-by-planet basis.

4.2 Mixed Envelopes

In this study we have not explicitly included mixed envelopes, with H₂O miscible in H/He. The difference in the radius obtained assuming a mixed vs an unmixed envelope is found to be less than the measured uncertainty in R_p of $\sim 0.1 R_\oplus$ for the majority of the Hycean candidates. This is in agreement with [Nixon & Madhusudhan \(2021\)](#) finding that 1% H₂O mixed in a H/He atmosphere has a minimal effect on the radius. They adopted a 5% envelope fraction, $T_0 = 500$ K, $P_0 = 0.1$ bar and $P_{rc} = 10$ bar, giving vapour or supercritical H₂O in the envelope to increase the likelihood of miscibility. It should be noted that for Hycean cases, the temperatures in the envelope are much less than considered by [Nixon & Madhusudhan \(2021\)](#), with a maximum of 400 K. The envelope mass fractions of Hycean worlds are also $\sim 10 - 100\times$ smaller than this. Therefore, the effect of the mixed envelope is expected to be even less. In their study of K2-18 b, [Madhusudhan et al. \(2020\)](#) find the median mixing ratio of H₂O to be 0.7–1.6% across the models considered. With such mixing ratios, they find the radius difference is less than half the measured uncertainty when a mixed envelope is considered. However, the recent study with JWST found a non-detection of H₂O ([Madhusudhan et al. 2023b](#)), differing from the previous study with HST due to degeneracy with CH₄. The low H₂O mixing ratio implies the presence of a tropospheric cold trap resulting in condensation, with H₂O possibly more abundant below ([Madhusudhan et al. 2023a,b](#)).

Therefore, given the current level of uncertainty in radius measurements, incorporating the effect of a mixed envelope into our calculations would introduce an extra source of degeneracy in determining interior compositions, while not significantly affecting results for possible ocean depths. JWST observations of Hycean candidates and sub-Neptunes generally can better constrain their H₂O mixing ratios. For instance, for TOI-270 d [Mikal-Evans et al. \(2023\)](#) found with HST a 99% credible upper limit of 30% for the mixing ratio of H₂O, which ruled out a steam atmosphere. Given precise estimates, we can adopt representative mixed envelope EOSs in future studies of these planets. JWST observations will allow more precise H₂O abundance estimates for both K2-18 b and TOI-270 d, and observations of other candidate Hycean worlds will reveal the diversity in H₂O abundance. We note that as uncertainties in R_p measurements improve with next-generation facilities, it could become important to consider the effect of mixed envelopes.

4.3 Future Directions for Internal Structure Modelling

A degenerate set of interior compositions can typically explain the bulk properties of an exoplanet in the sub-Neptune regime. Precise mass and radius measurements are therefore critical for internal structure modelling, as these can reduce the number of plausible solutions. This is evident from [Figure 7](#), and from the variation in possible H/He mass fractions for TOI-732 c based on the available sources for M_p and R_p measurements. The other essential avenue is atmospheric observations, which can help to break the degeneracy – this will be discussed further in [Section 4.4](#).

There are a number of assumptions made in our internal structure model, including our adopted EOSs, that may be investigated in the future. We do not consider the effect of hydrated silicate/iron layers, which was investigated in recent studies ([Shah et al. 2021](#); [Dorn & Lichtenberg 2021](#)). However, the effect on the $M-R$ relation for

solid rock in super-Earths was found to be smaller than the current typical precision of measurements ([Shah et al. 2021](#)). Furthermore, the behaviour of high-pressure ices is not fully known. This includes potential interactions between the high-pressure ices and underlying rock ([Vazan et al. 2022](#); [Kovačević et al. 2022](#)). [Vazan et al. \(2022\)](#) suggest that for the mass range $5 - 15 M_\oplus$, ice and rock can be mixed in the interiors of sub-Neptunes, but whether this occurs is dependent on the conditions at formation. We also note that the phase transitions and EOS of high-pressure ices are still very uncertain and require further study. Our H₂O EOS can be modified as new data becomes available. For instance, recent studies have revealed a new phase of ice VII known as ice VIII ([Grande et al. 2022](#)) which is suggested to have an effect on the $M-R$ relation comparable to observational uncertainties ([Huang et al. 2021](#)).

We have adopted an adiabatic profile throughout the H₂O layer, as is commonly assumed in internal structure models for sub-Neptune-sized planets (e.g. [Sotin et al. 2007](#); [Nixon & Madhusudhan 2021](#); [Leleu et al. 2021](#)). However, the presence of thermal boundary layers in the interior would form barriers to convection and could affect the permitted compositions. The effect of these layers has been explored for Uranus and Neptune (e.g. [Podolak et al. 2019](#)).

4.4 Observational Prospects

As we have shown in this paper, and has been discussed thoroughly in the literature (e.g. [Rogers & Seager 2010a](#); [Valencia et al. 2013](#); [Leleu et al. 2021](#); [Nixon & Madhusudhan 2021](#)), the bulk properties of a sub-Neptune are insufficient to place robust constraints on its composition, due to degenerate solutions. Atmospheric data are key for breaking these degeneracies. The first question for these planets will be establishing the presence or lack of an H₂-rich atmosphere. Atmospheric observations with HST and/or JWST have already confirmed H₂-rich atmospheres for K2-18 b ([Benneke et al. 2019](#); [Tsiaras et al. 2019](#); [Madhusudhan et al. 2023b](#)) and TOI-270 d ([Mikal-Evans et al. 2023](#)). However, even if the presence of an H₂-rich atmosphere is established, Hycean worlds can be degenerate with sub-Neptunes with either an H₂-rich envelope and a solid rocky surface, or with a deep H₂-rich atmosphere that causes the surface to be too hot to sustain liquid H₂O. The essential step in diagnosing a Hycean world is thus establishing the presence of the surface ocean. This requires precise abundances for a number of different molecules and a comprehensive exploration of the possible chemical pathways on the planet given these abundances. The key molecules are H₂O, CH₄, NH₃, CO₂ and CO, in addition to any other hydrocarbons present ([Yu et al. 2021](#); [Hu et al. 2021](#); [Tsai et al. 2021](#); [Madhusudhan et al. 2023a](#)). [Figure 8](#) in [Madhusudhan et al. \(2023a\)](#) summarises the route to chemically diagnosing a Hycean world via these molecules. In the recent study by [Madhusudhan et al. \(2023b\)](#), enhanced CH₄ and CO₂ were detected along with a lack of NH₃ in the observable atmosphere of K2-18 b, suggesting the presence of a surface ocean. This was carried out using JWST transmission spectra for one transit with each of NIRISS SOSS (Single Object Slitless Spectroscopy) and NIRSpec G395H. Additional upcoming JWST observations of K2-18 b, including one transit with MIRI LRS (Low Resolution Spectroscopy) via the same program (GO 2722) and multiple transits with NIRSpec G395H via GO 2372, can verify these detections.

The planets TOI-270 d, TOI-1468 c and TOI-732 c are also scheduled for spectroscopic observations with JWST in Cycle 2. For each planet, at least three transits will be observed, one with each of NIRISS SOSS, NIRSpec G395H and MIRI LRS; for TOI-270 d, additional NIRISS and NIRSpec observations will be obtained. These will be observed in multiple programs (GO 3557, GTO 2759, GO

4098). As discussed above, the same combination of observations is also being carried out for K2-18 b in multiple programs (GO 2722 and GO 2372). The predicted uncertainties and long wavelength coverage are expected to allow robust detections of the key molecules required to diagnose a Hycean planet. The observations are hence expected to aid the distinction of a Hycean world from scenarios of a rocky planet with a thick H/He envelope, mini-Neptune or water world as outlined above, akin to the initial findings for K2-18 b (Madhusudhan et al. 2023b). LHS 1140 b has also been observed as part of Cycle 1 GO Program 2334, with a transit observed with each of NIRSPEC G395H and G235H.

Hycean worlds are promising candidates for biomarker detection due to their larger radii and higher temperatures compared to rocky planets. Madhusudhan et al. (2021) investigated the observability of biomarkers in the atmospheres of Hycean candidates K2-18 b, TOI-270 d and TOI-732 c, considering DMS, CS₂, CH₃Cl, OCS and N₂O as biomarkers. They predicted that the approved observations of K2-18 b in Cycle 1 would be sufficient to detect biomarkers in its atmosphere if present in the quantities considered. Potential evidence for DMS in the atmosphere of K2-18 b was suggested by Madhusudhan et al. (2023b), though the abundance is not robustly constrained by the retrieval. They note the need for further theoretical exploration of atmospheric and interior processes when evaluating the viability of any possible biosignature. The additional observing time may better constrain the abundance in addition to potential detections of other species.

The prospect of identifying Hycean worlds amongst the exoplanet population and potentially detecting signs of life on them has recently become a tangible possibility. There remains the exciting potential for life's existence on a planet vastly different to our own. Additional theoretical studies in the future could help further develop our understanding of Hycean worlds and their ability to support life.

ACKNOWLEDGEMENTS

FR and NM acknowledge support from the Science & Technology Facilities Council (UKRI grant 2605554) towards the PhD studies of FR. We thank the anonymous reviewer for the careful review of our manuscript and helpful comments. FR thanks Matthew Nixon for model comparisons at the initial stage of the project.

DATA AVAILABILITY

This work is theoretical and no new data is generated as a result.

REFERENCES

- Alibert Y., 2014, *A&A*, **561**, A41
- Anderson O. L., Dubrovinsky L., Saxena S. K., LeBihan T., 2001, *Geophys. Res. Lett.*, **28**, 399
- Benneke B., et al., 2017, *ApJ*, **834**, 187
- Benneke B., et al., 2019, *ApJ*, **887**, L14
- Birch F., 1952, *J. Geophys. Res.*, **57**, 227
- Bitsch B., Raymond S. N., Buchhave L. A., Bello-Arufe A., Rathcke A. D., Schneider A. D., 2021, *A&A*, **649**, L5
- Blain D., Charnay B., Bézard B., 2021, *Astron. Astrophys.*, **646**, A15
- Bonfanti A., et al., 2024, *A&A*, **682**, A66
- Brugger B., Mousis O., Deleuil M., Deschamps F., 2017, *ApJ*, **850**, 93
- Cadieux C., et al., 2024, *ApJ*, **960**, L3
- Caillabet L., Mazevet S., Loubeyre P., 2011, *Phys. Rev. B*, **83**, 094101
- Chabrier G., Potekhin A. Y., 1998, *Phys. Rev. E*, **58**, 4941
- Chabrier G., Mazevet S., Soubiran F., 2019, *ApJ*, **872**, 51
- Charette M., Smith W., 2010, *Oceanography*, **23**, 112–114
- Chaturvedi P., et al., 2022, *Astronomy & Astrophysics*, **666**, A155
- Choblet G., Tobie G., Sotin C., Kalousová K., Grasset O., 2017, *Icarus*, **285**, 252
- Cloutier R., Menou K., 2020, *AJ*, **159**, 211
- Cloutier R., et al., 2019, *A&A*, **621**, A49
- Cloutier R., et al., 2020, *AJ*, **160**, 3
- Dittmann J. A., et al., 2017, *Nature*, **544**, 333
- Dorn C., Lichtenberg T., 2021, *ApJ*, **922**, L4
- Dorn C., Venturini J., Khan A., Heng K., Alibert Y., Helled R., Rivoldini A., Benz W., 2017, *A&A*, **597**, A37
- Dunaeva A. N., Antsyshkin D. V., Kuskov O. L., 2010, *Solar System Research*, **44**, 202
- Elkins-Tanton L. T., Seager S., 2008, *ApJ*, **685**, 1237
- Fei Y., Mao H., Hemley R. J., 1993, *J. Chem. Phys.*, **99**, 5369
- Feistel R., Wagner W., 2006, *Journal of Physical and Chemical Reference Data*, **35**, 1021
- Fortney J. J., Marley M. S., Barnes J. W., 2007, *ApJ*, **659**, 1661
- French M., Mattsson T. R., Nettelmann N., Redmer R., 2009, *Phys. Rev. B*, **79**, 054107
- Fulton B. J., Petigura E. A., 2018, *AJ*, **156**, 264
- Fulton B. J., et al., 2017, *AJ*, **154**, 109
- Gandhi S., Madhusudhan N., 2017, *MNRAS*, **472**, 2334
- Gardner J. V., Armstrong A. A., Calder B. R., Beaudoin J., 2014, *Marine Geodesy*, **37**, 1
- Genda H., 2016, *Geochemical Journal*, **50**, 27
- Grande Z. M., et al., 2022, *Phys. Rev. B*, **105**, 104109
- Grasset O., Schneider J., Sotin C., 2009, *ApJ*, **693**, 722
- Günther M. N., et al., 2019, *Nature Astronomy*, **3**, 1099
- Gupta A., Schlichting H. E., 2019, *MNRAS*, **487**, 24
- Gupta A., Schlichting H. E., 2020, *MNRAS*, **493**, 792
- Haldemann J., Alibert Y., Mordasini C., Benz W., 2020, *A&A*, **643**, A105
- Hardegree-Ullman K. K., Zink J. K., Christiansen J. L., Dressing C. D., Ciardi D. R., Schlieder J. E., 2020, *ApJS*, **247**, 28
- Hemley R., et al., 1987, *Nature*, **330**, 737–740
- Hernandez J.-A., Caracas R., Labrosse S., 2022, *Nature Communications*, **13**, 3303
- Hu R., Damiano M., Scheucher M., Kite E., Seager S., Rauer H., 2021, *ApJ*, **921**, L8
- Huang C., et al., 2021, *MNRAS*, **503**, 2825
- Huang C., Rice D. R., Steffen J. H., 2022, *MNRAS*, **513**, 5256
- Izidoro A., Schlichting H. E., Isella A., Dasgupta R., Zimmermann C., Bitsch B., 2022, *ApJ*, **939**, L19
- Journaux B., et al., 2020a, *Journal of Geophysical Research (Planets)*, **125**, e06176
- Journaux B., et al., 2020b, *Space Sci. Rev.*, **216**, 7
- Kalousová K., Sotin C., 2018, *Geophys. Res. Lett.*, **45**, 8096
- Kalousová K., et al., 2018, *Icarus*, **299**, 133
- Karki B. B., et al., 2000, *Phys. Rev. B*, **62**, 14750
- Kasting J. F., Whitmire D. P., Reynolds R. T., 1993, *Icarus*, **101**, 108
- Kaye L., et al., 2022, *MNRAS*, **510**, 5464
- Kite E. S., Ford E. B., 2018, *ApJ*, **864**, 75
- Kitzmann D., et al., 2015, *MNRAS*, **452**, 3752
- Klotz S., et al., 2017, *Phys. Rev. B*, **95**, 174111
- Knudson M. D., et al., 2012, *Phys. Rev. Lett.*, **108**, 091102
- Kovačević T., González-Cataldo F., Stewart S. T., Militzer B., 2022, *Scientific Reports*, **12**, 13055
- Lebec L., et al., 2023, *Icarus*, **396**, 115494
- Léger A., et al., 2004, *Icarus*, **169**, 499
- Leleu A., et al., 2021, *A&A*, **649**, A26
- Levi A., Sasselov D., Podolak M., 2017, *ApJ*, **838**, 24
- Lillo-Box J., et al., 2020, *A&A*, **642**, A121
- Lingam M., Loeb A., 2018, *Astron. J.*, **156**, 151
- Lopez E. D., Fortney J. J., Miller N., 2012, *ApJ*, **761**, 59
- Madhusudhan N., Lee K. K. M., Mousis O., 2012, *ApJ*, **759**, L40
- Madhusudhan N., Nixon M. C., Welbanks L., Piette A. A. A., Booth R. A., 2020, *ApJ*, **891**, L7

- Madhusudhan N., Piette A. A. A., Constantinou S., 2021, *ApJ*, **918**, 1
- Madhusudhan N., Moses J. I., Rigby F., Barrier E., 2023a, *Faraday Discussions*, **245**, 80
- Madhusudhan N., Sarkar S., Constantinou S., Holmberg M., Piette A. A. A., Moses J. I., 2023b, *ApJ*, **956**, L13
- Maruyama S., et al., 2013, *Geosci. Front.*, **4**, 141
- Meadows V. S., Barnes R. K., 2018, in Deeg H. J., Belmonte J. A., eds., *Handbook of Exoplanets*. p. 57, doi:10.1007/978-3-319-55333-7_57
- Ment K., et al., 2019, *AJ*, **157**, 32
- Merino N., et al., 2019, *Front. Microbiol.*, **10**, 780
- Mikal-Evans T., et al., 2023, *AJ*, **165**, 84
- Mousis O., Deleuil M., Aguichine A., Marcq E., Naar J., Aguirre L. A., Brugger B., Gonçalves T., 2020, *ApJ*, **896**, L22
- Nixon M. C., Madhusudhan N., 2021, *MNRAS*, **505**, 3414
- Noack L., et al., 2016, *Icarus*, **277**, 215
- Nowak G., et al., 2020, *A&A*, **642**, A173
- O'Malley-James J. T., Kaltenegger L., 2017, *MNRAS*, **469**, L26
- Owen J. E., Wu Y., 2013, *ApJ*, **775**, 105
- Owen J. E., Wu Y., 2017, *ApJ*, **847**, 29
- Petigura E. A., 2020, *AJ*, **160**, 89
- Piette A. A. A., Madhusudhan N., 2020, *ApJ*, **904**, 154
- Podolak M., Helled R., Schubert G., 2019, *MNRAS*, **487**, 2653
- Ramirez R. M., 2018, *Geosciences*, **8**, 280
- Ramirez R. M., Levi A., 2018, *MNRAS*, **477**, 4627
- Ricker G. R., et al., 2015, *Journal of Astronomical Telescopes, Instruments, and Systems*, **1**, 014003
- Rogers J. G., Owen J. E., 2021, *MNRAS*, **503**, 1526
- Rogers L. A., Seager S., 2010a, *ApJ*, **712**, 974
- Rogers L. A., Seager S., 2010b, *ApJ*, **716**, 1208
- Rogers L. A., Bodenheimer P., Lissauer J. J., Seager S., 2011, *ApJ*, **738**, 59
- Rogers J. G., Schlichting H. E., Owen J. E., 2023, *ApJ*, **947**, L19
- Rothschild L. J., Mancinelli R. L., 2001, *Nature*, **409**, 1092
- Salpeter E. E., Zapolsky H. S., 1967, *Physical Review*, **158**, 876
- Saumon D., Chabrier G., van Horn H. M., 1995, *ApJS*, **99**, 713
- Seager S., Kuchner M., Hier-Majumder C. A., Militzer B., 2007, *ApJ*, **669**, 1279
- Selsis F., Kasting J. F., Levrard B., Paillet J., Ribas I., Delfosse X., 2007, *A&A*, **476**, 1373
- Shah O., Alibert Y., Helled R., Mezger K., 2021, *A&A*, **646**, A162
- Shields A. L., Ballard S., Johnson J. A., 2016, *Phys. Rep.*, **663**, 1
- Sotin C., Grasset O., Mocquet A., 2007, *Icarus*, **191**, 337
- Thomas S. W., Madhusudhan N., 2016, *MNRAS*, **458**, 1330
- Tremblay L., Line M. R., Stevenson K., Kataria T., Zellem R. T., Fortney J. J., Morley C., 2020, *AJ*, **159**, 117
- Tsai S.-M., Innes H., Lichtenberg T., Taylor J., Malik M., Chubb K., Pierre-humbert R., 2021, *ApJ*, **922**, L27
- Tsiaras A., Waldmann I. P., Tinetti G., Tennyson J., Yurchenko S. N., 2019, *Nature Astronomy*, **3**, 1086
- Valencia D., Sasselov D. D., O'Connell R. J., 2007, *ApJ*, **665**, 1413
- Valencia D., Guillot T., Parmentier V., Freedman R. S., 2013, *ApJ*, **775**, 10
- Van Eylen V., et al., 2021, *MNRAS*, **507**, 2154
- Vazan A., Sari R., Kessel R., 2022, *ApJ*, **926**, 150
- Venturini J., Guilera O. M., Haldemann J., Ronco M. P., Mordasini C., 2020, *A&A*, **643**, L1
- Vinet P., et al., 1989, *J. Phys. Condensed Matter*, **1**, 1941
- Wagner W., Pruß A., 2002, *Journal of Physical and Chemical Reference Data*, **31**, 387
- Wunderlich F., et al., 2019, *A&A*, **624**, A49
- Yang J., Cowan N. B., Abbot D. S., 2013, *ApJ*, **771**, L45
- Yu X., Moses J. I., Fortney J. J., Zhang X., 2021, *ApJ*, **914**, 38
- Zeng L., Sasselov D., 2013, *PASP*, **125**, 227
- Zeng L., et al., 2019, *Proceedings of the National Academy of Science*, **116**, 9723
- de Pater I., Lissauer J. J., 2010, *Planetary Sciences*. Cambridge University Press

This paper has been typeset from a $\text{\TeX}/\text{\LaTeX}$ file prepared by the author.